Journal of the Meteorological Society of Japan, Vol. 72, No. 6, pp. 901–935, 1994

Kelvin and Mixed Rossby-Gravity Waves Appearing in the GFDL "SKYHI" General Circulation Model and the FGGE Dataset: Implications for Their Generation Mechanism and Role in the QBO

By Y. Hayashi and D.G. Golder

Geophysical Fluid Dynamics Laboratory/NOAA, Princeton University, Princeton, New Jersey, U.S.A.

(Manuscript received 9 June 1994, in revised form 3 October 1994)

Abstract

To evaluate simulations and theories of equatorial Kelvin and mixed Rossby-gravity (MRG) waves, and to gain insight into their generation mechanism and role in the quasi-biennial oscillation, a space-time spectral analysis is performed on output data from the 40-level, three-degree latitude GFDL "SKYHI" general circulation model and on the GFDL FGGE dataset.

The SKYHI and FGGE stratospheric Kelvin waves are dominated by an eastward-moving, wavenumber-one, 10–20-day period component in the lower stratosphere. These waves are accompanied by higher wavenumber-frequency components, which can be detected more clearly in the upper stratosphere than in the lower stratosphere. On the other hand, the SKYHI and FGGE MRG waves are dominated by a westward-moving, wavenumber 3–5, 4–6-day component in the lower stratosphere. These waves are dominated by lower-wavenumbers (1–2) and shorter periods (2–4 days) in the upper stratosphere. The amplitudes of the SKYHI/FGGE Kelvin and MRG waves are comparable to those estimated from observed (non-FGGE) station data, whereas the SKYHI model produces only a very weak quasi-biennial oscillation. The SKYHI precipitation data intermittently exhibit grid-size pulses of precipitation, but do not clearly exhibit spectral peaks which correspond to Kelvin and MRG waves.

On the basis of the present analysis, it is proposed that Kelvin, MRG, and gravity waves result from wave-convection interactions and are intermittently triggered by random pulses of convective heating. It is speculated that the quasi-biennial oscillation is produced primarily by gravity waves and will increase in amplitude with horizontal resolution, as grid-size pulses of convective heating and small-scale gravity waves are more adequately produced in the model.

1. Introduction

The tropical atmosphere is known to be associated with certain distinct periodicities other than the seasonal and diurnal cycles. Among them are the 4–5-day easterly wave, the 4–5-day mixed Rossby-gravity (MRG) wave, the 10–20-day Kelvin wave, and the 40–50- and 25–30-day tropical intraseasonal oscillations. Reviews of observed MRG and Kelvin waves has been presented by Wallace (1971, 1973) and Yanai (1975), while a recent review of observed tropical intraseasonal oscillations has been presented by Madden and Julian (1994). A brief review of theories of tropical transient waves relevant to the present study can be found in Hayashi and Golder (1993).

a. The mixed Rossby-gravity wave

The MRG wave was discovered in the equatorial lower stratosphere by Yanai and Maruyama (1966) while searching for disturbances which would vertically transport momentum to account for the quasi-biennial oscillation (QBO) of the zonal wind in the lower stratosphere. Maruyama (1967) showed that this wave moves westward with a zonal wavelength of about 10,000 km (wavenumber four) and a period of 4–5 days, tilting westward with height with a vertical wavelength of 5–10 km. It takes the form of vortices centered over the equator, resembling the theoretical MRG wave discussed by Matsuno (1966).

The MRG wave was also observed in the equatorial troposphere (Yanai *et al.*, 1968). The tropospheric MRG wave differs from easterly waves in structure and preferred location (Nitta 1970; Takayabu and Nitta 1993). The MRG wave was found to transport both momentum and energy up-

ward into the stratosphere (Maruyama 1968, Yanai and Hayashi 1969). In spite of the vertical transport of westerly momentum, the theoretical MRG wave results in an acceleration of the mean easterly flow (Hayashi 1970). This results from the vertical momentum flux convergence being dominated by the Coriolis acceleration due to mean meridional circulations, which are induced by the wave heat flux. This easterly acceleration is consistent with the effective vertical momentum flux (Lindzen 1970) or the more general EP flux (Andrews and McIntyre 1976), which involves the fluxes both of momentum and heat. It is believed that the MRG wave accounts for the easterly phase of the QBO. The observed MRG wave is associated with the energy conversion from available potential energy generated by tropospheric heating (Nitta 1970, 1972).

The MRG wave has been simulated by an 11-level GFDL general circulation model (Hayashi 1974) and a 12-level NCAR model (Tsay 1974). Hayashi and Golder (1978) demonstrated, using an idealized GFDL model, that the MRG wave appears even in the absence of geographical effects. In the absence of extratropical disturbances, its amplitude is greatly reduced. Furthermore, without condensational heating, the MRG wave was found to disappear. It was concluded that the simulated MRG wave is primarily generated by condensational heating and enhanced by extratropical disturbances. Hayashi and Golder (1980) further demonstrated that the seasonal amplification of the simulated MRG wave is related to extratropical disturbances. Zangvil and Yanai (1980, 1981) and Yanai and Lu (1983) found that a pronounced equatorward flux of wave energy accompanied the observed MRG wave. Itoh and Ghil (1988) showed, using a numerical model with moist convective adjustment, that equatorially asymmetric forcing from middle latitude disturbances enhances MRG waves.

b. The Kelvin wave

The Kelvin wave was first observed in the tropical lower stratosphere by Wallace and Kousky (1968). This wave moves eastward with zonal wavenumber one and a period of 10–20 days, tilting eastward with height with a vertical wavelength of 5–10 km. It is characterized by its wind vectors being directed parallel to the equator, resembling the theoretical Kelvin wave of Matsuno (1966). The observed Kelvin wave transports both momentum and energy upward into the stratosphere (Wallace and Kousky 1968, Maruyama 1969). In contrast to the MRG wave, the Kelvin wave theoretically results in a westerly acceleration. It is believed that this wave accounts for the westerly phase of the QBO (*e.g.*, Holton and Lindzen 1972).

The Kelvin wave was simulated by an 11-level GFDL general circulation model (Hayashi 1974) and a 12-level NCAR model (Tsay 1974). Hayashi and Golder (1978) demonstrated, using an idealized GFDL model, that the Kelvin wave appears even in the absence of geographical effects. In contrast to the MRG wave, its amplitude was hardly affected in the absence of extratropical disturbances. In the absence of condensational heating, the Kelvin wave was found to disappear, similar to the results for the MRG wave. It was concluded that the simulated Kelvin wave is generated by condensational heating, but not appreciably affected by extratropical disturbances.

In addition to the lower stratospheric Kelvin wave, Hirota (1978, 1979) observed an upper stratospheric Kelvin wave, which is also characterized by wavenumber one, but with shorter periods of 5–10 days and a longer vertical wavelength of 20–25 km than the lower-stratospheric Kelvin wave. Subsequently, Salby *et al.* (1984) observed a mesospheric Kelvin wave of wavenumber one but shorter periods of 3–4 days and a longer vertical wavelength of 30–50 km than the upper-stratospheric Kelvin wave. These shorter-period Kelvin waves were simulated by the 40-level SKYHI model (Hayashi *et al.*, 1984), and have been related to the simulated semiannual oscillation in the tropical middle atmosphere (Hamilton and Mahlman 1988).

c. Tropical intraseasonal oscillations

The tropical intraseasonal oscillation discovered by Madden and Julian (1971) is associated with wavenumber one and propagates eastward with a period of 40–50 days. It is also associated with a 180-degree phase reversal between the upper- and lower-tropospheric zonal velocities, taking the form of the Walker (zonal-vertical) circulation (Madden and Julian 1972).

The 40–50-day oscillation was adequately simulated by a GFDL R30 (30 zonal wavenumbers) spectral general circulation model (Hayashi and Golder 1986, 1988, 1993) and the SKYHI model (Hayashi and Golder 1993). The simulated 40–50-day oscillation was found to be accompanied by a 25–30-day oscillation having a comparable magnitude. The SKYHI model results indicate that the 25–30-day oscillation has a greater penetration of its amplitude into the stratosphere and a longer vertical wavelength in the lower stratosphere than the 40–50 day oscillation (Hayashi and Golder 1993). The 25–30-day oscillation can also be found in observed data (Hayashi and Golder 1986; Hartmann *et al.*, 1992), although it is much weaker, on the long-term average, than that simulated (Hayashi and Golder 1993). It was suggested (Hayashi and Golder 1993) that the 25–30-day oscillation is a lower vertical mode than the 40–50-day oscillation, but higher than the 10–20-day Kelvin wave. The 40–50 and 25–30 day oscillations, however, may not contribute to the QBO,

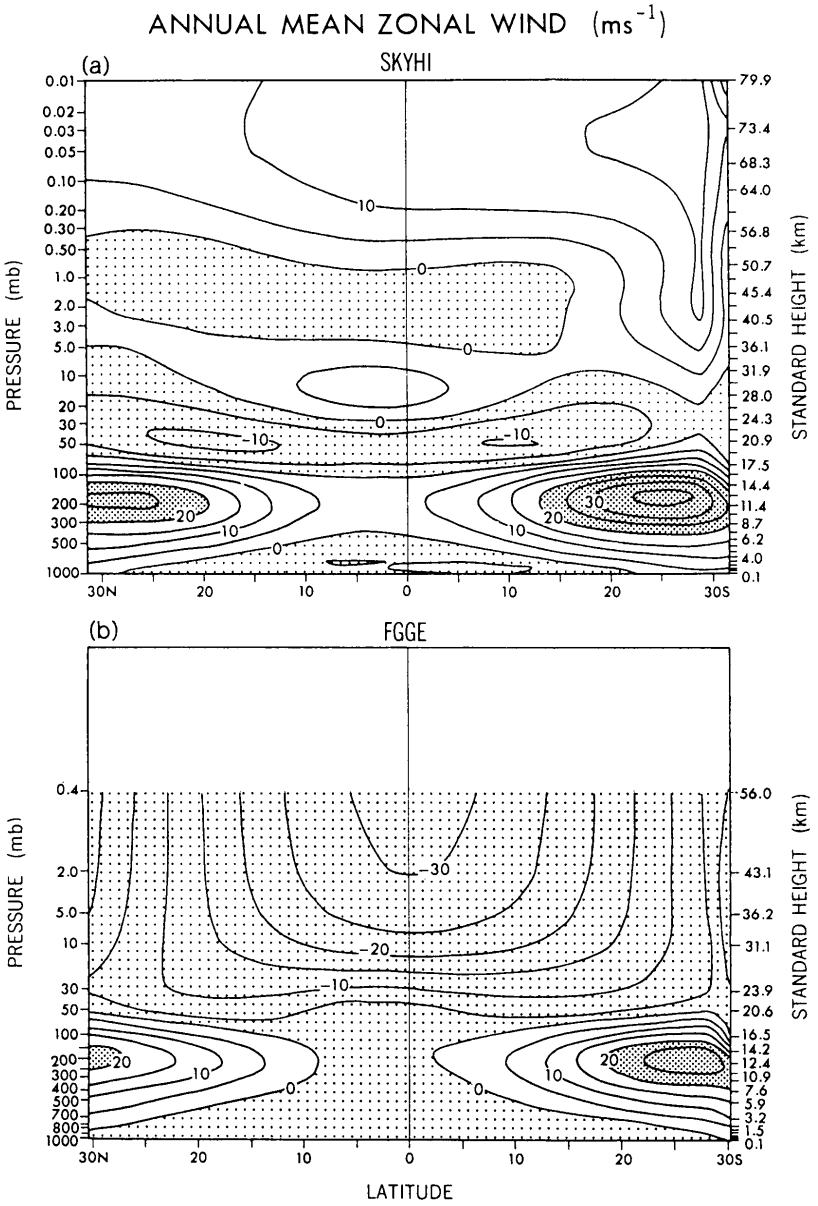

Fig. 1. (a) Latitude-height distribution (three-year average) of the annual mean zonal wind (m/s) of the 40-level, N30 (3 degree mesh) GFDL SKYHI general circulation model with seasonal variations. The levels of the finite-difference model are indicated by the standard heights. (b) As in Fig. 1a except for the GFDL FGGE data (December 1978–November 1979). The levels of the model used for four-dimensional assimilation are indicated by both the pressures and standard heights. No data are available above the model's highest level (56 km).

since their amplitudes are essentially confined to the troposphere.

d. The quasi-biennial oscillation

Mechanistic models have demonstrated that the QBO might result from wave-mean flow interactions involving either gravity waves (Lindzen and Holton 1968) or Kelvin and MRG waves (Holton and Lindzen 1972). Current general circulation models, however, simulate only a very weak QBO (*e.g.*, Hamilton *et al.*, 1994; Carilolle *et al.*, 1993). This may be due to a deficiency in the amplitudes of the Kelvin and MRG waves and/or gravity waves produced by the model.

An 11-level GFDL GCM adequately simulated Kelvin and MRG waves during the period July through August (Hayashi 1974), while a 12-layer NCAR model adequately simulated the Kelvin wave but severely underestimated the MRG wave during January (Tsay 1974). Recently, Manzini and Hamilton (1993) examined stratospheric tropical waves during a 60 day (April 18–June 16) integration of the

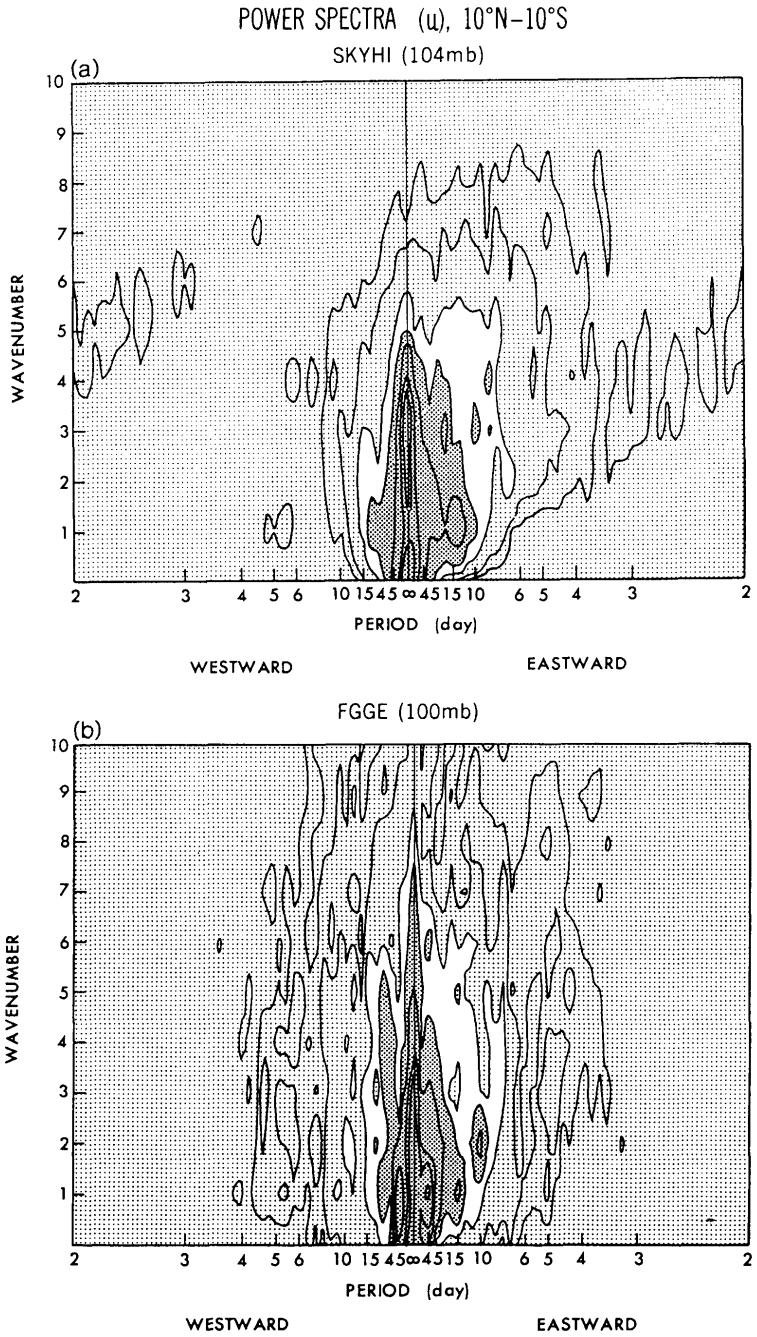

Fig. 2. Wavenumber-frequency distributions of the space-time power spectral density of the zonal velocity averaged over 10°N–10°S for (a) the SKYHI model at the 104-mb level and (b) the FGGE data at the 100-mb level. The contour values are 1, 2, 5, 10, 20, 50, 100, and 200 (10 m^2 s^{-2} day). Dark shade indicates values greater than 10, light shade values less than 5.

40-level GFDL SKYHI model. The amplitudes of the simulated wavenumbers 1–2 Kelvin waves were found to be slightly lower than those quoted for typical observed amplitudes by Wallace and Kousky (1968), while the zonal wavenumbers 3–4 MRG amplitudes were considerably smaller than those indicated by the original observations of Yanai and Maruyama (1966). On the other hand, Boville and Randel (1992) concluded that both Kelvin and MRG waves are adequately simulated during the period July through October by the current high-vertical-resolution NCAR model.

The above conclusions may be subject to the temporal length of the data, since the amplitudes of Kelvin and MRG waves are intermittent and undergo seasonal and interannual variations (Hayashi and Golder 1980; Maruyama 1991). To evaluate the amplitudes of the simulated waves in relation to the

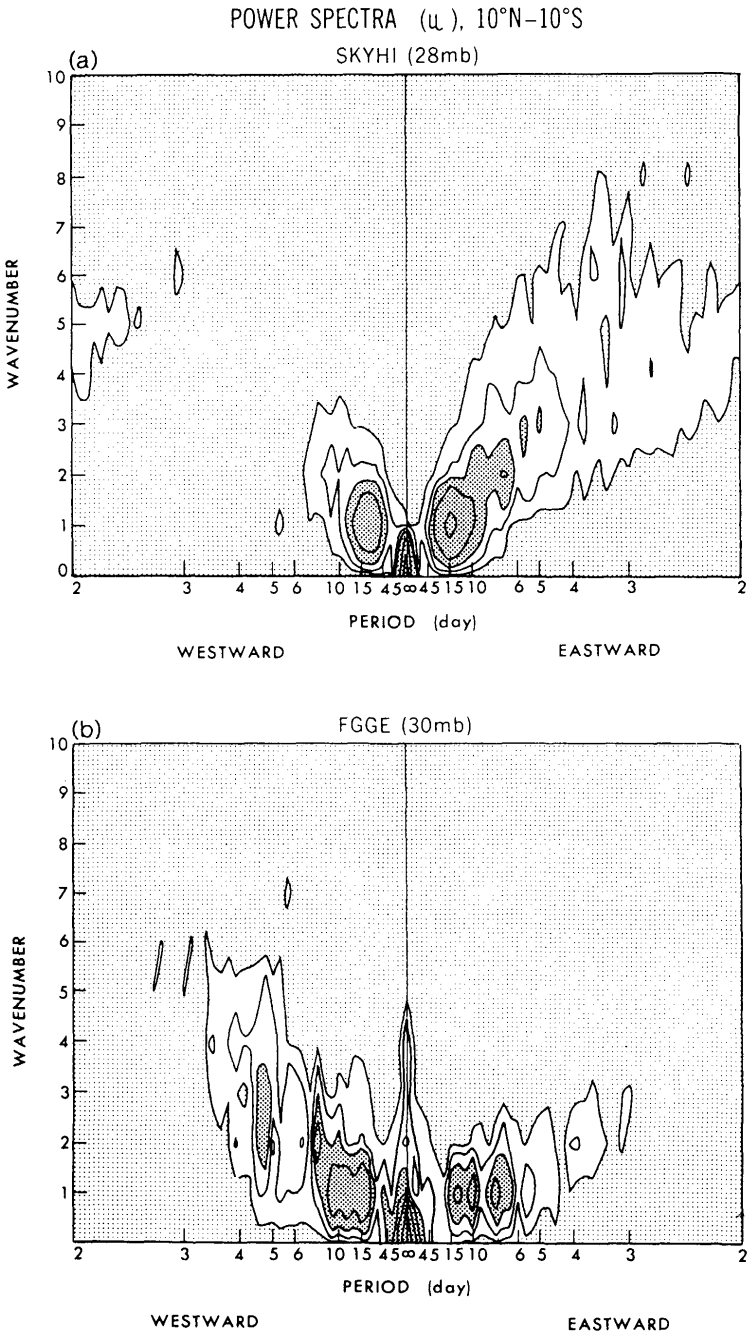

Fig. 3. As in Fig. 2, except for (a) the SKYHI model at the 28-mb level and (b) the FGGE data at the 30-mb level. Contour values: 2, 5, 10, 20, and 50 (10 m^2 s^{-2} day). Dark shade > 10, light shade < 2.

QBO, it would be more appropriate to use an entire-year dataset rather than a few months worth of data. Moreover, caution should be used in estimating the amplitudes of these waves from space-time spectra and time spectra, since the space-time amplitude is much smaller than the maximum value of longitudinally varying time amplitude (see Appendix B).

The present paper is intended to evaluate simulations and theories of Kelvin and MRG waves in comparison with observed data, and to gain insight into the generation mechanism and role of these waves in the QBO. To accomplish this, a space-time spectral analysis was conducted on three years of output data from the SKYHI model and the GFDL four-dimensional dataset for the FGGE year. Section 2 describes the model and observed data. Sections 3 and 4 analyze Kelvin and MRG waves, respectively. Conclusions and implications are given in Section 5.

2. Model and observed data

The general circulation model analyzed in the present study is the 40-level GFDL "SKYHI" model extending from the surface to about 0.01 mb (80 km) and includes the troposphere, stratosphere, and mesosphere with a horizontal resolution of N30 (3.0° latitude by 3.6° longitude). The model's physical processes include moist convective adjustment (Manabe *et al.*, 1965), surface hydrology, a planetary boundary layer, and radiation. Also included are orography, and imposed annual cycle of insolation, climatological set of seasonal sea-surface temperatures, and climatological cloudiness. However, neither the parameterized drag due to the orographically forced gravity waves nor the diurnal cycle of solar insolation is incorporated. Details of this model can be found in Fels *et al.* (1980), Levy *et al.* (1982), Hamilton and Mahlman (1988), and Manzini and Hamilton (1993). Results obtained from this model have been described in Mahlman and Sinclair (1980), Mahlman and Umscheid (1984, 1987), Andrews *et al.* (1983), Hayashi *et al.* (1989), Miyahara *et al.* (1986), Hamilton and Mahlman (1988), Hayashi *et al.* (1989), and Manzini and Hamilton (1993).

The simulated data analyzed here were sampled once daily from the model,which had been integrated over three model years. The model data were analyzed by the use of space-time spectrum and filter analyses. For comparison purposes, the same analyses were performed on the FGGE IIIb dataset (four-dimensional assimilation) processed by the use of an 18-level general circulation model at GFDL (see Ploshay *et al.*, 1983) during the FGGE observational period from December 1978 through November 1979. These data are, however, not available above 56 km.

Space-time spectral analysis (see Hayashi 1982) reveals wavenumber-frequency spectral distributions, as well as the statistical structure of the eastward- and westward-moving components for a given wavenumber and period. The space-time spectra were estimated by use of the maximum entropy method (see Hayashi 1982). Since the present spectral analysis makes use of an entire year of data, it is not necessary to remove the seasonal cycle prior to the spectral analysis.

Space-time filter analysis (see Hayashi and Golder 1986) reveals the zonal propagation and the wave patterns. The data, which are filtered for a given wavenumber and period range, can be composited, being phase-shifted for the desired eastward or westward phase velocities. The compositing acts to enhance the chosen eastward or westward component, depending on the direction of the phase shift. The space filtering and time filtering were accomplished by the use of a zonal Fourier decomposition and a recursive filter (see Murakami 1979), respectively. The frequency response of a 10–20-day band-pass recursive filter, for example, is designed in such a way that the amplitudes corresponding to 10 and 20 day periods are halved, while it is almost unchanged at a period of 15 days.

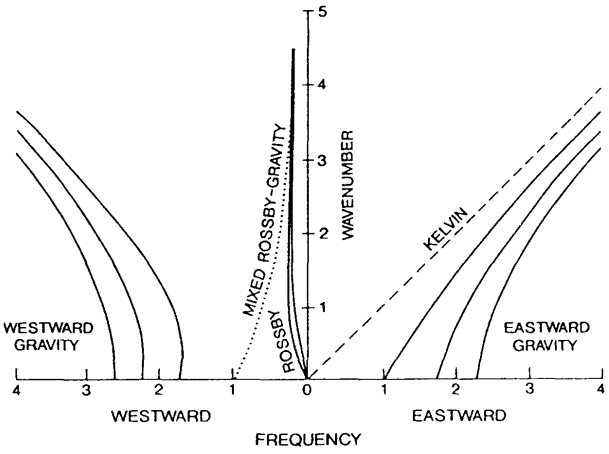

Fig. 4. Dispersion diagram for equatorial normal modes adapted from Matsuno (1966, Fig. 3a). The curves show the relationship between the non-dimensionalized wavenumber and frequency for Kelvin and mixed Rossby-gravity modes, Rossby modes, and eastward- and westward-moving gravity modes.

Figure 1 shows the latitude-height distributions of the annual-mean zonal wind of the SKYHI model and FGGE data. The model (Fig. 1a) exhibits equatorial easterlies and westerlies appearing alternately with height, whereas the FGGE data (Fig. 1b) exhibit equatorial easterlies throughout the depth of the atmospheric domain. The discrepancy in the model stratosphere is due to the lack of a realistic quasi-biennial oscillation. The westerlies in the simulated equatorial troposphere and the easterlies in the observed troposphere result from a small residual of local easterlies and westerlies, which are canceled in the zonal mean.

3. Kelvin waves

a. Wavenumber-frequency distributions

Figure 2 displays the wavenumber-frequency distributions near 100 mb of the space-time power spectral density of the SKYHI (a) and FGGE (b) zonal velocities averaged over 10°N–10°S. In both diagrams, a spectral peak of comparable magnitude can be seen at wavenumber one and an eastward-moving period of 15 days. These peaks are consistent with the zonal scale and period of the stratospheric equatorial Kelvin wave observed by Wallace and Kousky (1968).

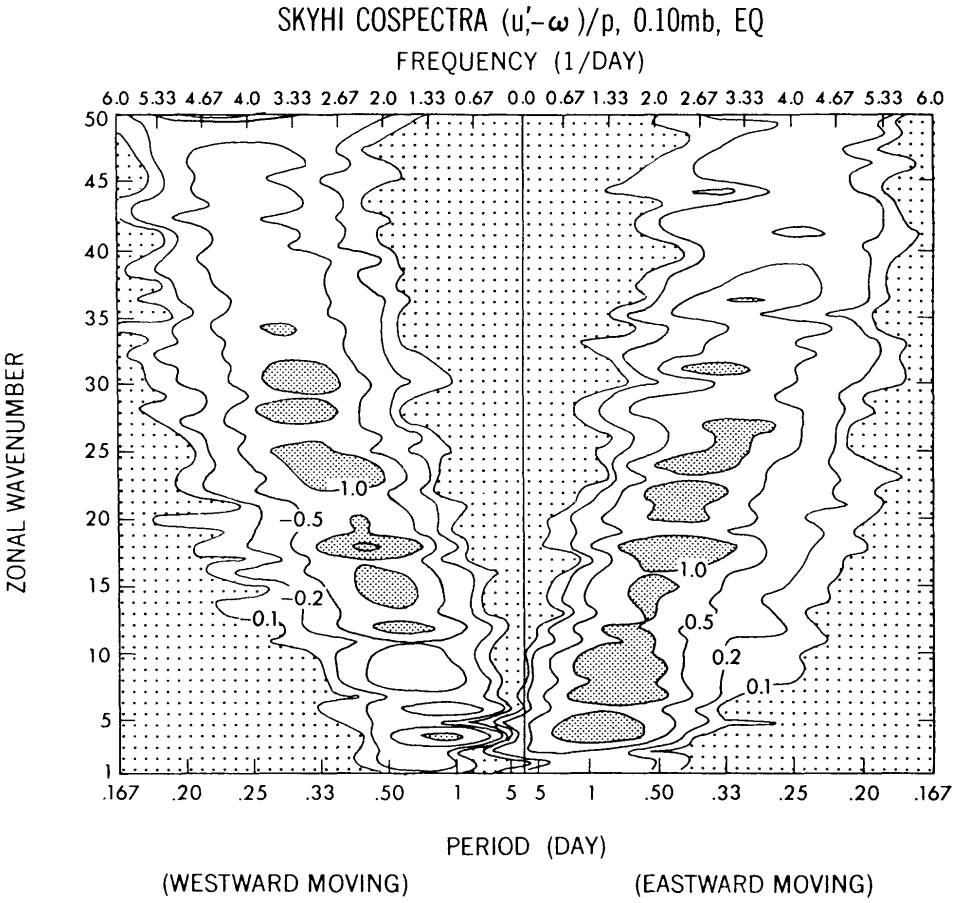

Fig. 5. Wavenumber-frequency distribution (wavenumber 1–50, period > 0.167 days) of the cospectral density (10^{-6} m s^{-2} day) of the vertical flux of zonal momentum ($-\overline{u'w'}/p$) at 0.10 mb (= 66.0 km) over the equator during December 20–27 of the N90 SKYHI model (adapted from Hayashi *et al.*, 1989). Only 1–50 out of 0–150 wavenumber components are shown. Contour values: −2.0, −1.0, −0.5, −0.1, 0.1, 0.2, 0.5, 1.0. Dark shade indicates absolute values greater than 1.0, while light shade indicates absolute values less than 0.1.

Figure 3 is the same as Fig. 2 except for a higher level at 30 mb. Figure 3a (SKYHI model), as well as Fig. 2a, reveals the existence of higher wavenumber-frequency components for eastward-moving periods. It is seen that the typical frequency of these components increases with wavenumber, qualitatively consistent with the dispersion relation (see Fig. 4) of the theoretical Kelvin mode. Recently, Maruyama (1994) found a two-day Kelvin wave in the equatorial stratosphere. The high wavenumber-frequency components at 30 mb are more pronounced than those at 100 mb. The increase in these components with height is consistent with the theoretical Kelvin wave in that the high-frequency component has a greater vertical group velocity (see Hayashi 1976, Fig. 5) and a more efficient upward propagation than the low-frequency component. The group velocity of Kelvin waves is roughly proportional to frequency as well as phase velocity (see Appendix A, Eq. A3b). Figure 3a also reveals a substantial westward-moving component at wavenumber one and 15–30 days, which corresponds to observed external Rossby waves (*i.e.*, the so-called 16-day wave, Madden 1978). The FGGE data (Fig. 3b) reveal more pronounced westward-moving than eastward-moving components.

To examine the wavenumber-frequency distribution over a much wider range, Fig. 5 shows the wavenumber-frequency spectral distribution (wavenumber 1–50, period > 0.167 days) for the cospectral density of the vertical momentum flux at 0.10 mb over the equator, during the period December 20–27 of the N90 SKYHI model, making use of hourly data (adapted from Hayashi *et al.*, 1989; Fig. 10b). It is seen that for wavenumbers greater than 20, the eastward- and westward-moving components of the vertical momentum flux have comparable magnitudes and opposite signs, being consistent with eastward- and westward-moving gravity waves. The net momentum flux due to these gravity waves plays a more important role in SKYHI simulations of the semiannual oscillation (SAO) of the

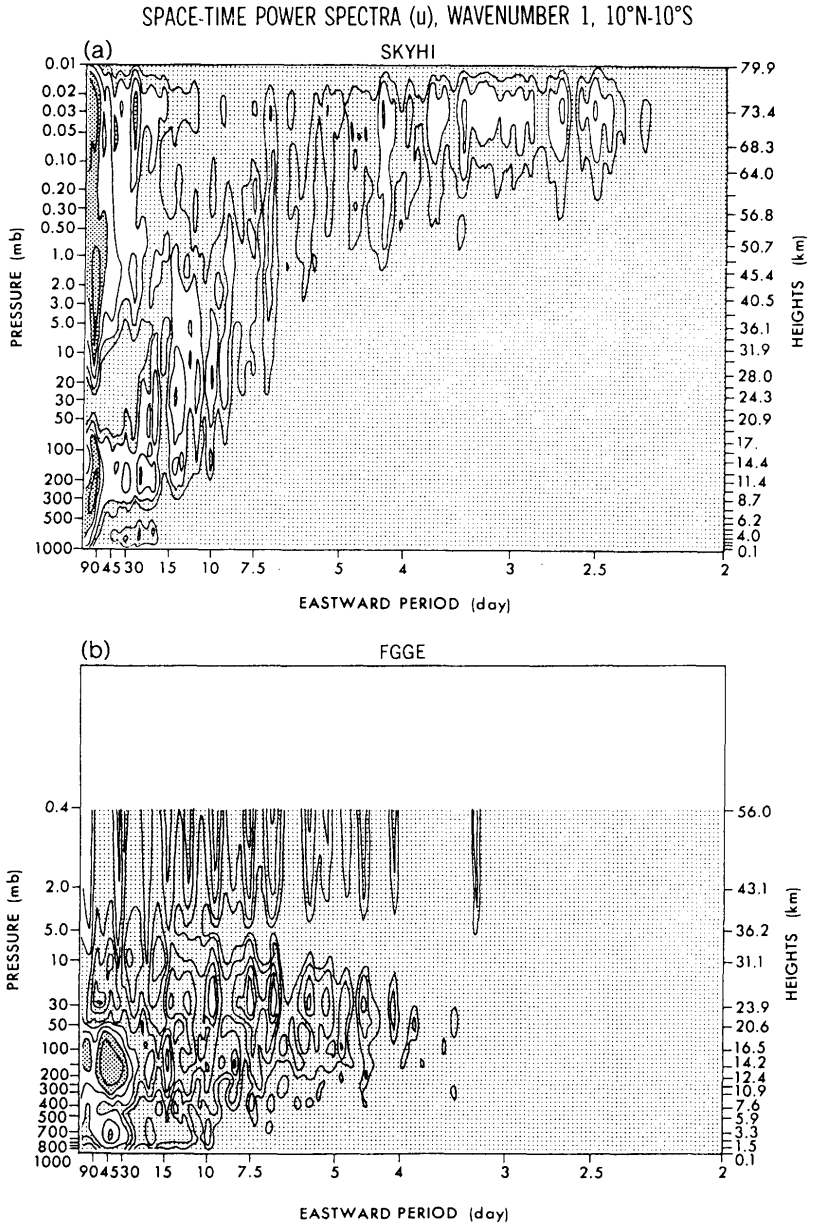

Fig. 6. Frequency-height distributions (wavenumber one) of the space-time power spectral density of the zonal velocity averaged between 10°N–10°S for (a) the SKYHI model and (b) the FGGE data. Only the eastward-moving components are shown. Contour values: 2, 5, 10, 20, 50, 100, and 200 (m^2 s^{-2} day). Dark shade > 100, light shade < 20.

tropical middle atmosphere than that due to Kelvin waves (Hamilton and Mahlman 1988). A careful inspection of Fig. 5 also reveals that, for wavenumbers 1–5 and periods longer than 2 days, the eastward-moving component is associated with a larger momentum flux than the westward-moving component, being consistent with the dominance of eastward-moving Kelvin waves.

Figure 6 compares the frequency-height distributions of the SKYHI (a) and FGGE (b) power spectral density of wavenumber-one zonal velocities averaged between 10°N–10°S. Only the eastward-moving components are shown. In the upper troposphere (around 200 mb) of the SKYHI model, spectral peaks are seen at periods of 40–50 and 25–30 days, corresponding to observed and simulated tropical 40–50- and 25–30-day oscillations (Hayashi and Golder 1993). The 40–50-day peak is confined to the troposphere, while the 25–30-day peak penetrates into the lower stratosphere. This contrast is consistent with the vertical group velocity of theoretical Kelvin waves consisting of different vertical modes, which increases with frequency for the same wavenumber (see Appendix A, Eq. A3c).

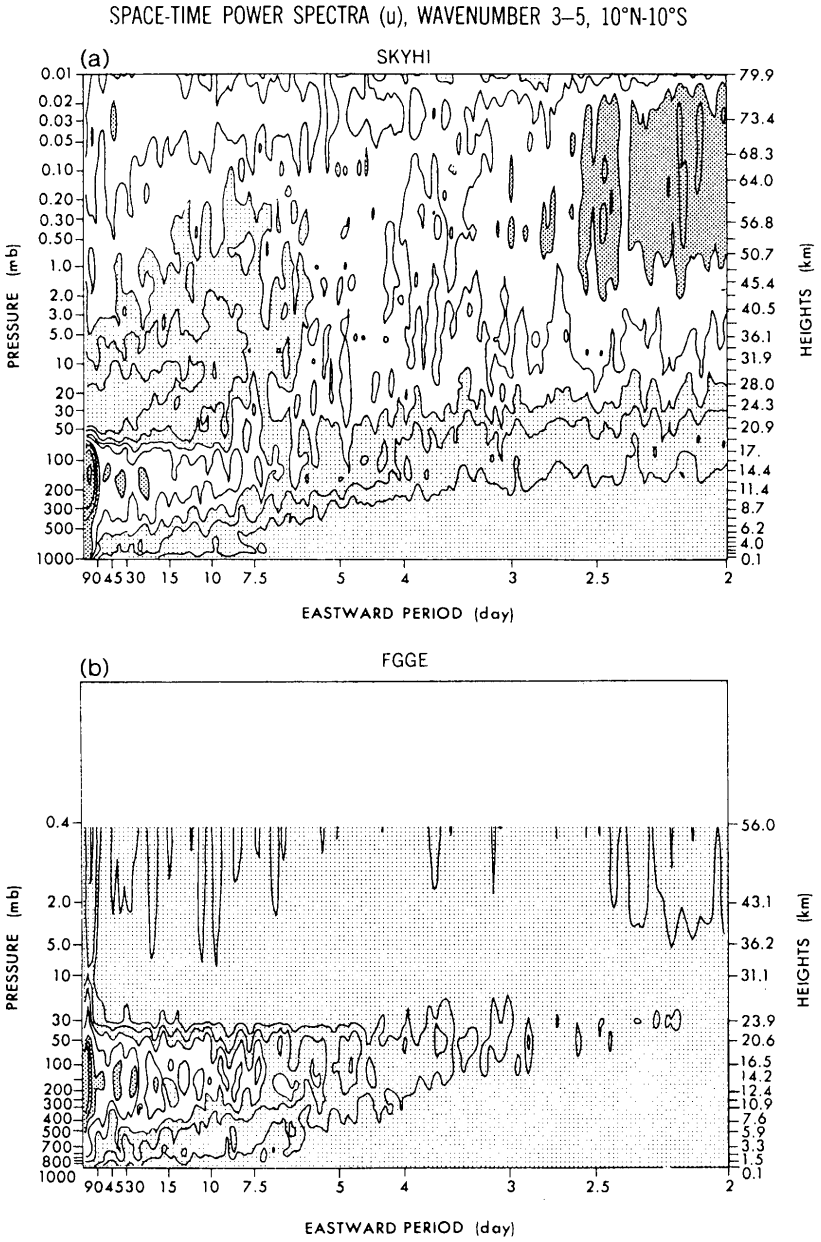

Fig. 7. As in Fig. 6, except for wavenumbers 3–5 and different shading. Contour values: 2, 5, 10, 20, 50, 100, 200, and 500 (m^2 s^{-2}). Dark shade > 50, light shade < 10.

In the upper troposphere and lower stratosphere, a 10–15-day peak can also be seen, which corresponds to observed stratospheric Kelvin waves. At higher levels, the wavenumber-one component exhibits spectral peaks at shorter periods. These spectral peaks correspond to upper-stratospheric and mesospheric Kelvin waves observed by Hirota (1979) and Salby *et al.* (1984) and simulated by the SKYHI model (Hayashi *et al.*, 1984). In the FGGE data, however, these peaks are not clearly seen, probably owing to the coarse vertical resolution.

Figure 7 is the same as Fig. 6 except for the wavenumber 3–5 components. As in the wavenumber-one component, the dominant frequency in the model is found to increase with height (Fig. 7a). In contrast to the model results, the high-frequency components in the stratosphere can not be clearly seen in the FGGE data (Fig. 7b), due to the coarse vertical resolution.

Since conventional spectral analyses of observed tropical data are mostly based on station data, Fig. 8 displays frequency-height distributions of the SKYHI (a) and FGGE (b) time power-spectral density (averaged over 150°E–150°W and 5°N–5°S) of the zonal velocity consisting of wavenumber 0–10 components. For both the SKYHI and FGGE results, the time spectral density values at 10–20-day periods in the lower stratosphere are about 100–200

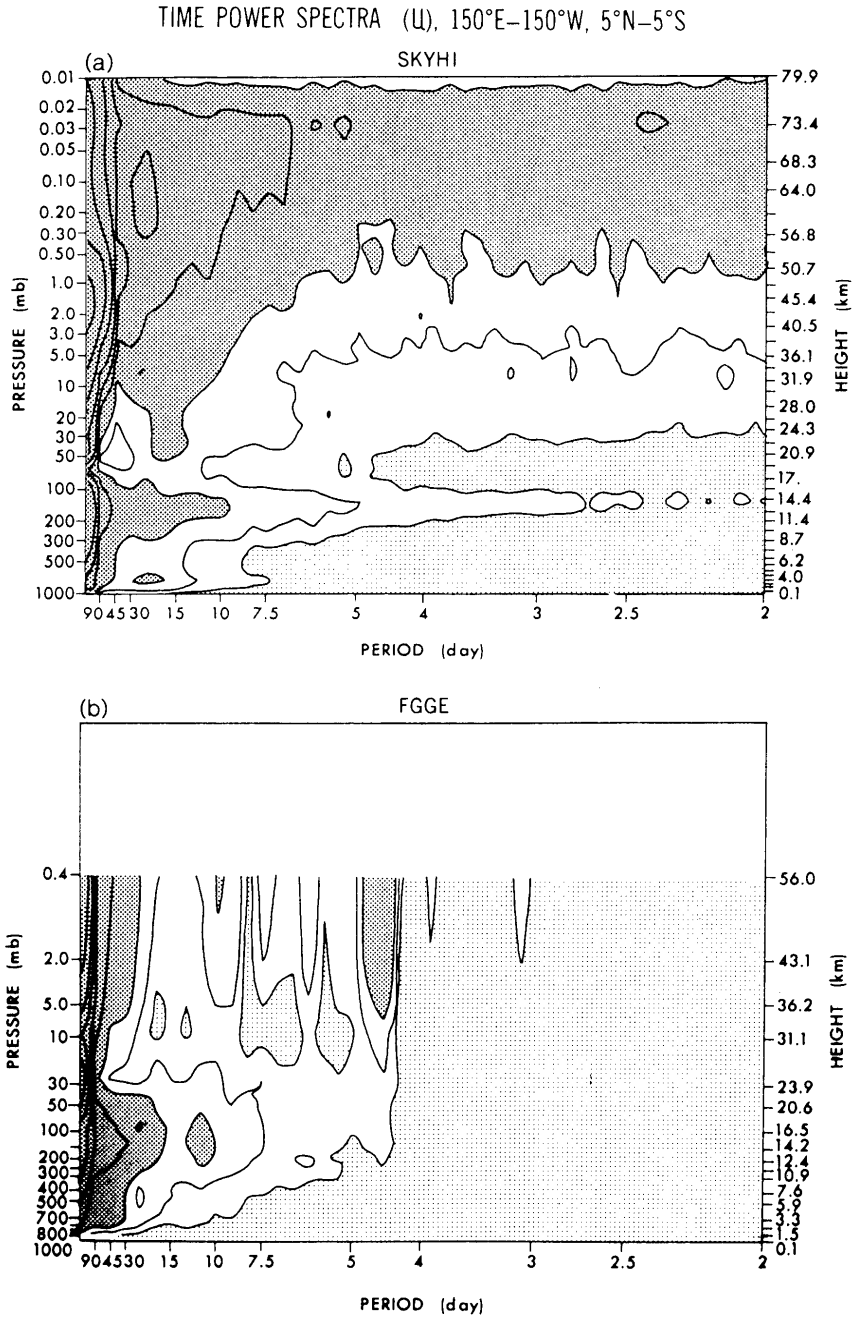

Fig. 8. Frequency-height distributions of (a) the SKYHI and (b) the FGGE time power spectral densities (averaged over 150°E–150°W, 5°N–5°S) of the zonal velocity consisting of the wavenumber 0–10 components. Contour values: 50, 100, 200, 500, 1000, 2000, and 5000 (m^2 s^{-2} day). Dark shade > 200, light shade < 50.

$(m/s)^2$ day. These values are almost the same for each year of the SKYHI data (not illustrated) and are comparable to an observed value (Yanai and Murakami 1970a) based on station data at Canton Island (2°S, 171°W). The amplitude calculated from the time power-spectral density over the 10–20-day period range is about 4 m/s, which is somewhat less than the value quoted for a typical amplitude of the observed Kelvin wave by Wallace (1973).

On the other hand, for both SKYHI and FGGE (Figs. 6a, 6b), the space-time spectral density values for wavenumber-one at periods of 10–20 days (eastward moving) in the lower stratosphere are only 20–50 $(m/s)^2$ day, which is 4–5 times smaller than the time spectral density. This discrepancy is due to the presence of multiple-wavenumber components in the time spectra. These components result from Kelvin waves being localized, and substantially contribute

(a)

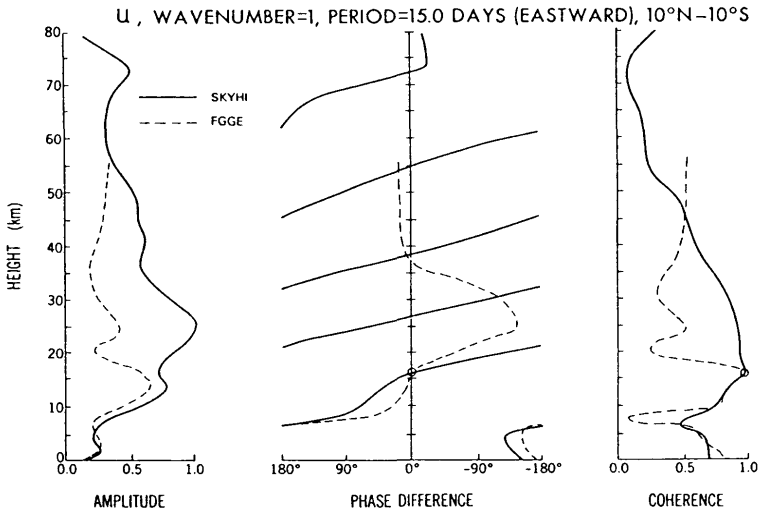

(b)

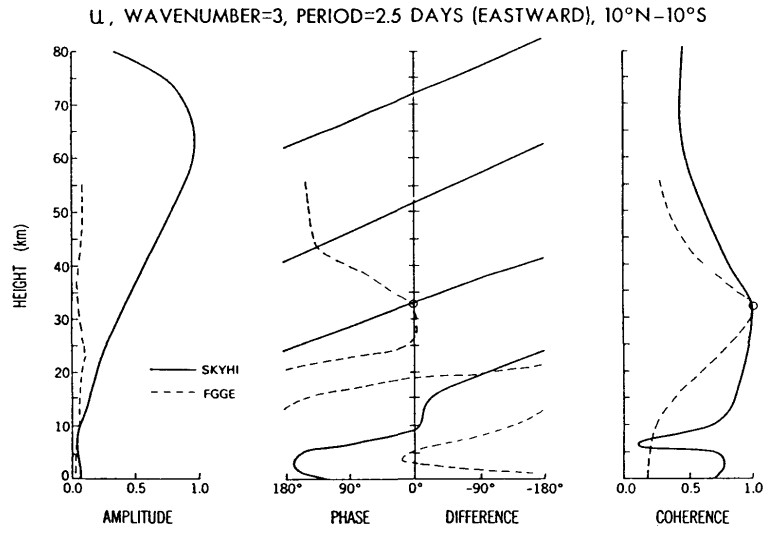

Fig. 9. (a) Vertical distributions of the space-time amplitude (normalized by the maximum SKYHI value), phase difference, and coherence (wavenumber one, eastward-moving 15.0-day period) of the zonal velocity averaged between 10°N–10°S for the SKYHI model (solid lines) and the FGGE data (dashed lines). The reference level (16 km) for the phase difference and coherence is indicated by open circles. (b) As in Fig. 9a except for the wavenumber three, eastward-moving 2.5-day period, and reference level of 32 km.

to the time power spectra as is explained mathematically in Appendix B. The wavenumber-one space-time spectra are similar to the time spectra consisting of only the wavenumber-one component (not illustrated).

b. Vertical structure

Figure 9a shows the vertical distributions of space-time amplitude, phase difference, and coherence of the wavenumber one, eastward-moving, 15-day-period component of the zonal velocity, averaged between 10°N–10°S for the SKYHI model (solid lines) and the FGGE data (dashed lines). The reference level for the phase difference and coherence is located around 16 km. The amplitude reaches a maximum around 25 km in the SKYHI distribution and around 13 km for FGGE. The decrease of the FGGE amplitude above 13 km is probably due to the coarse vertical resolution. The SKYHI phase-line tilts eastward with height from 5 to 50 km, with a typical vertical wavelength of 15 km. Owing to the coarse vertical resolution above 25 km, the FGGE data exhibit a similar phase tilt only between 5 and 25 km. The eastward tilt of Kelvin waves with height theoretically implies an upward transport of energy and momentum (Lindzen and Matsuno, 1968). The low value of vertical coherence at higher levels in the model is probably due to the amplitude of the Kelvin wave being dominated

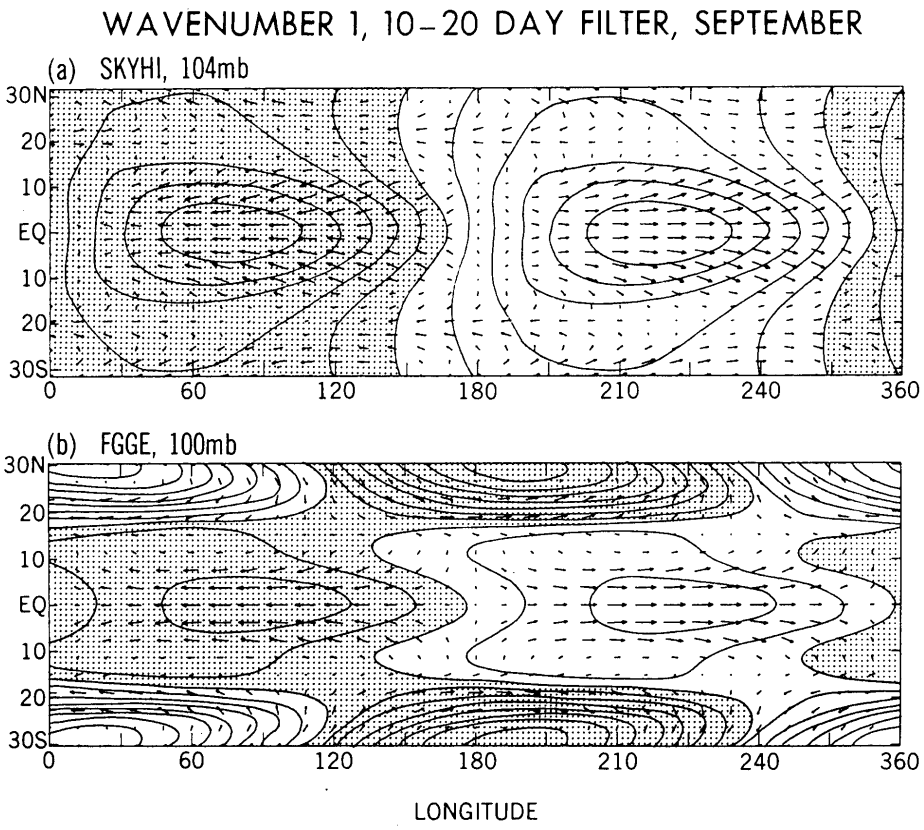

Fig. 10. Longitude-latitude sections of the wavenumber-one component of frequency-filtered wind vectors and geopotential height contours for (a) the SKYHI model at the 104-mb level and (b) the FGGE data at the 100-mb level. The 10–20 day filtered data have been composited over one month (September) along the longitude-time isoline of 31 m/s eastward phase velocity. The data have been further modified to extract the equatorially symmetric component of the zonal velocity and geopotential and the equatorially antisymmetric component of the meridional velocity. Shading indicates positive contour values. The longitudes indicate only relative position. The latitudinal scale and the meridional component have been enlarged by a factor of 2 relative to the longitudinal scale and the zonal component, respectively.

by the eastward-moving component that is nonlinearly produced by westward-moving external Rossby waves as noted in Figs. 3a and 3b.

The structure of the simulated and observed wavenumber-one component for shorter periods ("fast Kelvin waves") can be found in Hayashi *et al.* (1984) and Salby *et al.* (1984), respectively. Figure 9b is the same as Fig. 9a except for the wavenumber-three, eastward-moving 2.5-day-period component. The reference level is around 32 km. The amplitude is seen to increase with height in both the SKYHI and FGGE distributions. The SKYHI phaselines (solid lines) tilt eastward with height above 15 km, with a typical vertical wavelength of 20 km. This tilt can be detected, even above 50 km, in contrast to the wavenumber-one component. This contrast is due to the wavenumber-three component having a greater penetration into the mesosphere and a larger signal-to-noise ratio than the wavenumber-one component. On the other hand, the FGGE phaseline (dashed lines) exhibits an eastward tilt only below 20 km.

c. Horizontal structure

Figure 10 consists of longitude-latitude sections near 100 mb of the wavenumber-one 10–20-day filtered wind vectors and geopotential contours of (a) the SKYHI model and (b) the FGGE data. (The longitude marks denote only relative location). The filtered data have been composited daily during the month of September along the longitude-time isoline of 31 m/s eastward phase velocity, corresponding to wavenumber one and a 15-day period. September was chosen for the compositing presented here, since both the SKYHI and FGGE Kelvin-wave patterns appear distinctly during this month. To enhance Kelvin modes, the equatorially symmetric component was extracted for the zonal velocity and geopotential while the equatorially antisymmetric component was extracted for the meridional velocity (see Yanai and Murakami 1970b for the procedure of the

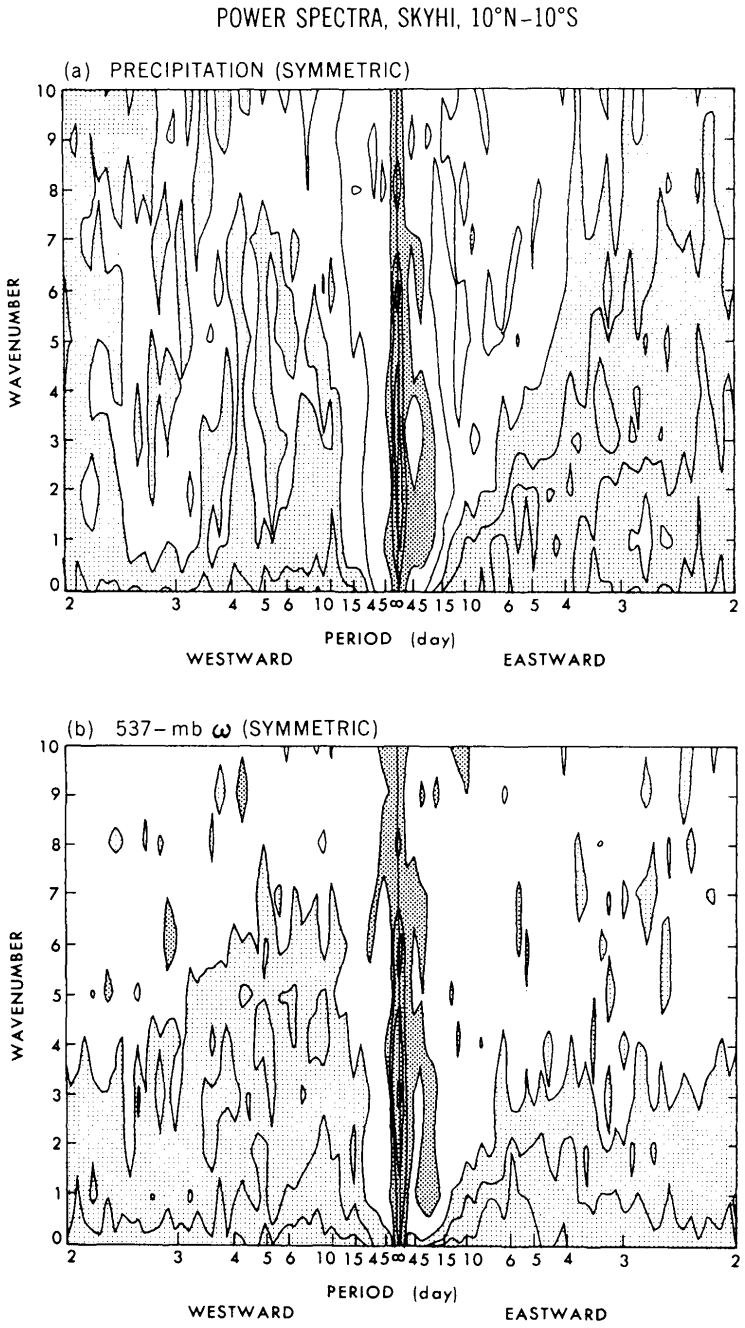

Fig. 11. Wavenumber-frequency distributions of the space-time power spectral density of the equatorially symmetric component of (a) the precipitational heating and (b) the 537-mb vertical pressure velocity averaged over 10°N–10°S of the SKYHI model. Contour values: (a) 5, 10, 20, 50, 100, 200, and 500 (23.4 W^2 m^{-4} day). Dark shade > 100, light shade < 20. (b) 5, 10, 20, 50, 100, 200, and 500 (10 Pa^2 s^{-2} day). Dark shade > 50, light shade < 20.

decomposition).

The SKYHI and FGGE patterns between 10°N–10°S resemble the theoretical Kelvin mode (see Matsuno 1966, Fig. 8), which is characterized by geopotential height contours centered over the equator, wind vectors directed parallel to the equator, and the zonal component varying with longitude in phase with the geopotential height. The cause of the considerable discrepancy between the SKYHI and FGGE patterns at 10°–30° latitudes is unknown. The wavenumber-three component with a 2–3 day filter also exhibits the Kelvin-mode pattern between 10°N–10°S (not illustrated).

d. Precipitation and evaporation

Figure 11 displays the SKYHI wavenumber-frequency distribution of the equatorially symmet-

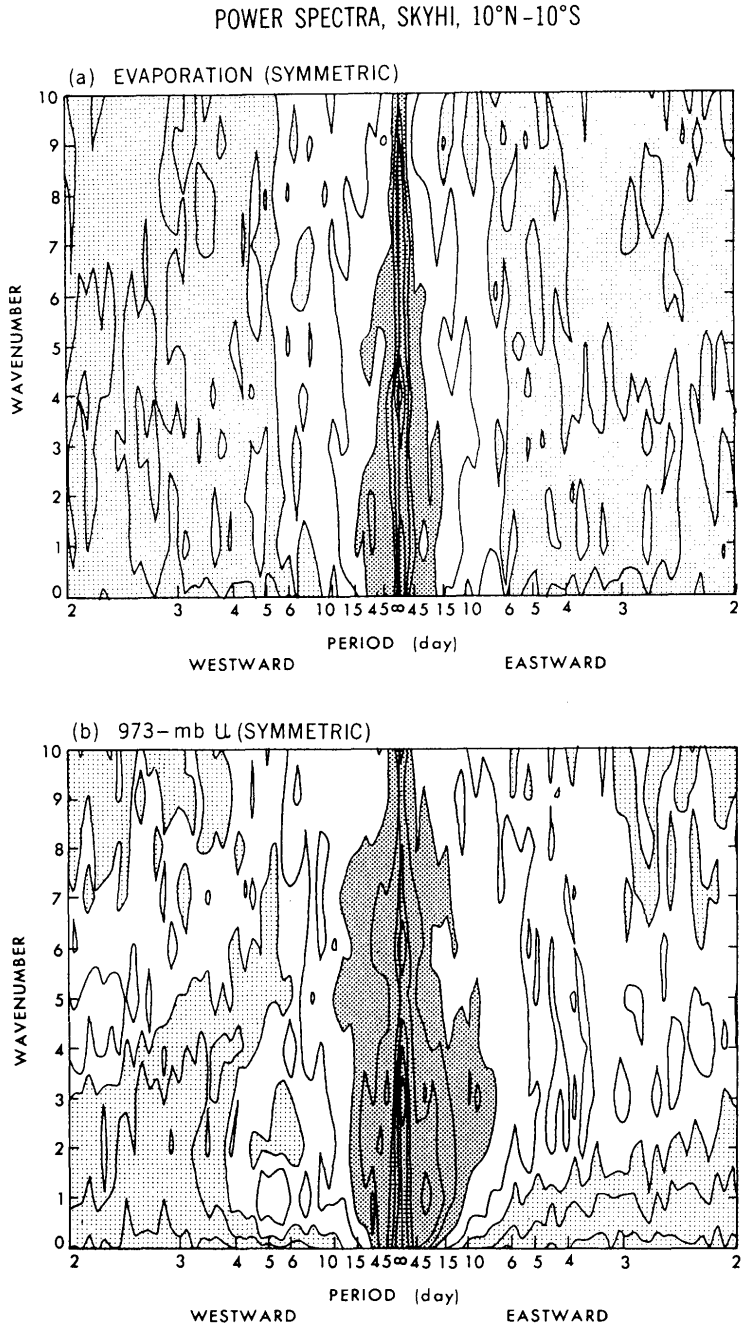

Fig. 12. As in Fig. 11 except for (a) the evaporational heating and (b) the 973-mb zonal velocity. Contour values: (a) 2, 5, 10, 20, 50, 100, 200, and 500 (2.34 W^2 m^{-4} day). Dark shade > 50, light shade < 10. (b) 2, 5, 10, 20, 50, 100, 200, 500, and 1000 (0.01 m^2 s^{-2} day). Dark shade > 50, light shade < 20.

ric component of (a) precipitation and (b) the 537-mb vertical pressure-velocity averaged over 10°N–10°S. The theoretical Kelvin mode is characterized by equatorially symmetric zonal and vertical velocities. The frequency-spectral distributions of precipitation and vertical velocity are roughly that of red noise; that is, there is no distinct spectral peak which would correspond to the eastward-moving, wavenumber-one, 10–20-day Kelvin wave. This result is consistent with previous analyses of an 11-level GFDL general circulation model (Hayashi 1974) and the N30 SKYHI model (Manzini and Hamilton 1993). This conclusion is contrary to wave-CISK theory (Hayashi 1970; Lindzen 1974) which predicts that both convective heating and vertical velocity have distinct periods in the absence of random noise. This result also is contrary to the maximum response of equatorial waves to random

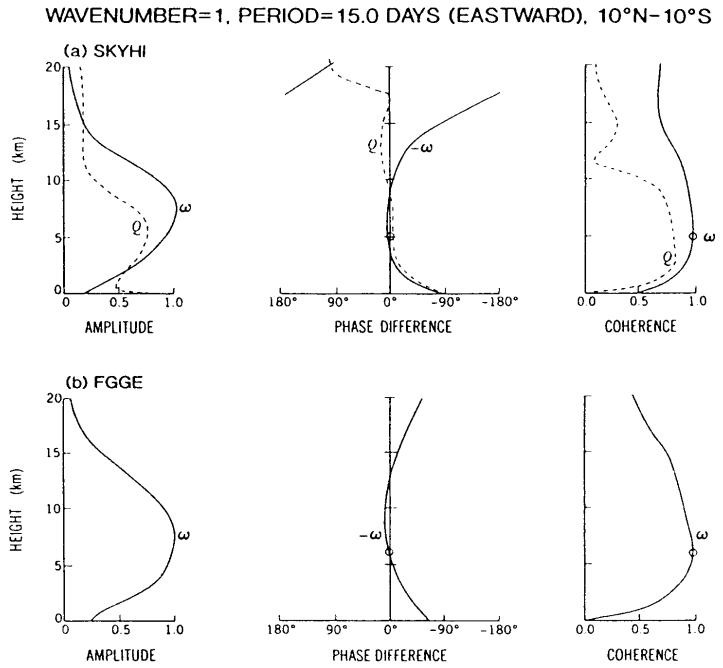

Fig. 13. (a) Vertical distributions of the normalized space-time amplitude, phase difference, and coherence (wavenumber one, period 15 days, eastward moving) of the vertical pressure velocity (ω, solid lines) and convective-adjustment heating (Q, dashed lines) averaged between 10°N–10°S of the SKYHI model. The phase difference and coherence are measured with reference to $-\omega$ (open circles) at 537 mb. (b) As in Fig. 13a except for the FGGE data. Convective heating is not available from the FGGE dataset. The phase difference and coherence are measured with reference to $-\omega$ (open circles) at 500 mb.

thermal forcing (Holton 1973; Hayashi 1976; Chang 1976; Itoh 1977) in which the vertical velocity forced by random heating has a distinct periodicity. Precipitation is not available in the FGGE dataset.

Figure 12 shows the wavenumber-frequency distribution (SKYHI model) of the symmetric component of (a) evaporation and (b) the 973-mb zonal velocity averaged over 10°N–10°S. Neither the evaporation nor the 973-mb zonal velocity exhibits a distinct spectral peak at an eastward-moving period of 10–20 days, contrary to evaporation-wind feedback theory (Neelin *et al.*, 1987; Emanuel 1987) in which both evaporation and winds should have a distinct period if there is no background noise. Evaporation is not available from the FGGE dataset.

Figure 13a shows the SKYHI vertical distributions (up to 20 km) of the normalized space-time amplitude, phase difference, and coherence (wavenumber one, eastward-moving 15.0-day period) of the equatorially symmetric component of vertical pressure-velocity (ω) and convective heating (Q) averaged between 10°N–10°S. The phase difference and coherence were measured with respect to $-\omega$ around 5 km. The maximum amplitudes of Q and ω are found to occur in the middle troposphere, contrary to traditional wave-CISK theory, in which the heating maximum is prescribed in the upper troposphere to explain the observed 10–20-day Kelvin waves. When the heating maximum is prescribed in the middle troposphere, the period of wave-CISK Kelvin waves lengthens to 25–30 days (*e.g.*, see Takahashi 1987) for a strong heating parameter. (For a weak parameter, the period can be 10–20 days, but the growth rate is zero.)

It is also seen that Q and $-\omega$ are nearly in phase in the troposphere, being consistent with wave-CISK theory. However, this phase relationship is contrary to random thermal-forcing theory (Holton 1973; Hayashi 1976; Chang 1976; Itoh 1977; Salby and Garcia 1987; Garcia and Salby 1987) which predicts a quadrature-phase relationship, as pointed out by Hayashi (1976). Both Q and ω tilt westward with height in the lower troposphere. A similar westward tilt of ω also occurs in the FGGE data (Fig. 13b). Convective heating is, however, not available in the FGGE dataset. The westward tilt of Q and ω can be found also in simulated intraseasonal oscillations (Hayashi and Golder 1988, 1993). The phase tilt of ω probably results from boundary-layer convergence and results in a phase lag between mid-tropospheric convective heating and low-level convergence. The vertical tilt of Q is contrary to both wave-CISK and random thermal-forcing theories, which assume no vertical phase variation in Q.

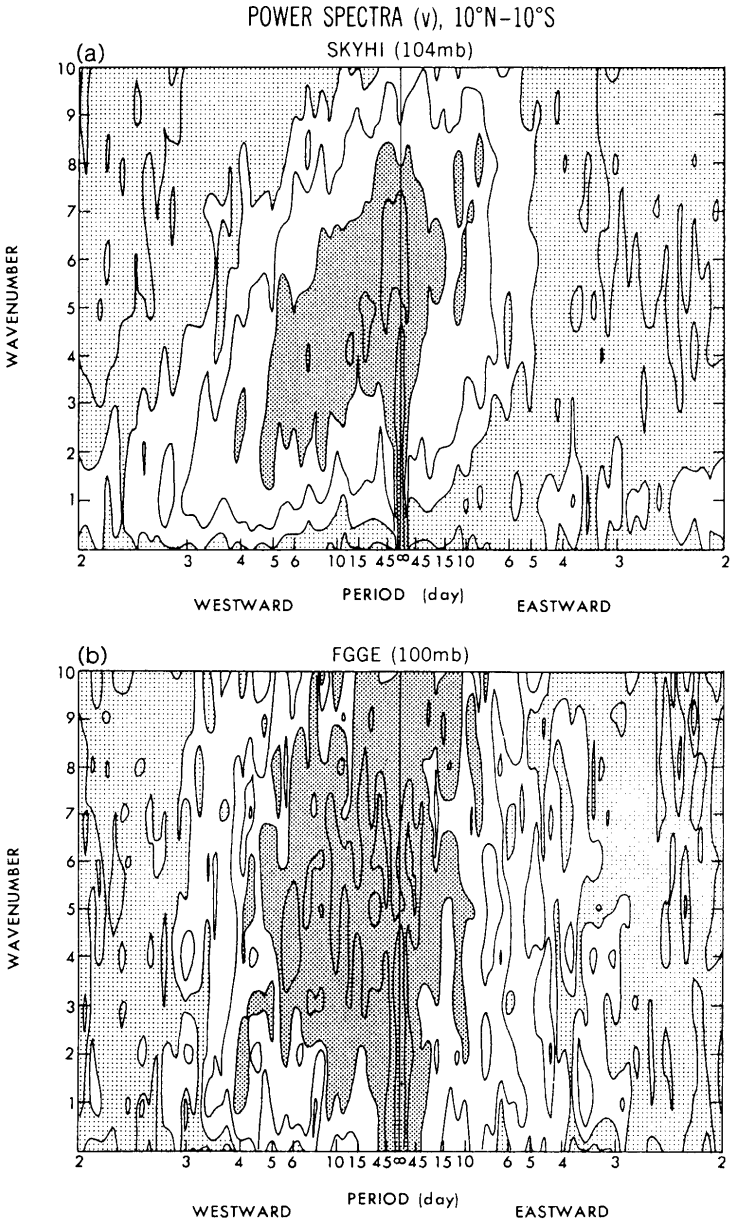

Fig. 14. Wavenumber-frequency distributions of the space-time power spectral density of the meridional velocity averaged over 10°N–10°S for (a) the SKYHI model at 104 mb and (b) the FGGE data at 100 mb. The contour values are 1, 2, 5, 10, 20, 50, 100, and 200 (0.1 m^2 s^{-2} day). Dark shade indicates values greater than 20, light shade values less than 5.

4. Mixed Rossby-gravity waves

a. Wavenumber-frequency distributions

Figure 14 displays wavenumber-frequency distributions near 100 mb of the space-time power spectral density of (a) the SKYHI and (b) the FGGE meridional velocities averaged over 10°N–10°S. The SKYHI spectra are associated with stronger westward than eastward moving components; the dominant period increasing with wavenumber, consistent with the dispersion relation (see Fig. 4) of the theoretical MRG mode. The FGGE spectra are also associated with stronger westward than eastward moving components, although the increase of the period with wavenumber is not as clear as in the SKYHI spectra. The FGGE spectral peak at wavenumber 4 and periods of 5–6 days, which corresponds to the observed lower-stratospheric MRG wave (Yanai and Maruyama 1966), has a magnitude comparable to that of the SKYHI spectra.

At a higher level (47.9 mb), the low-wavenumber and high-frequency components of the SKYHI meridional wind spectra (Fig. 15a) are more pronounced. This is consistent with low-wavenumber and high-frequency components of theoretical MRG

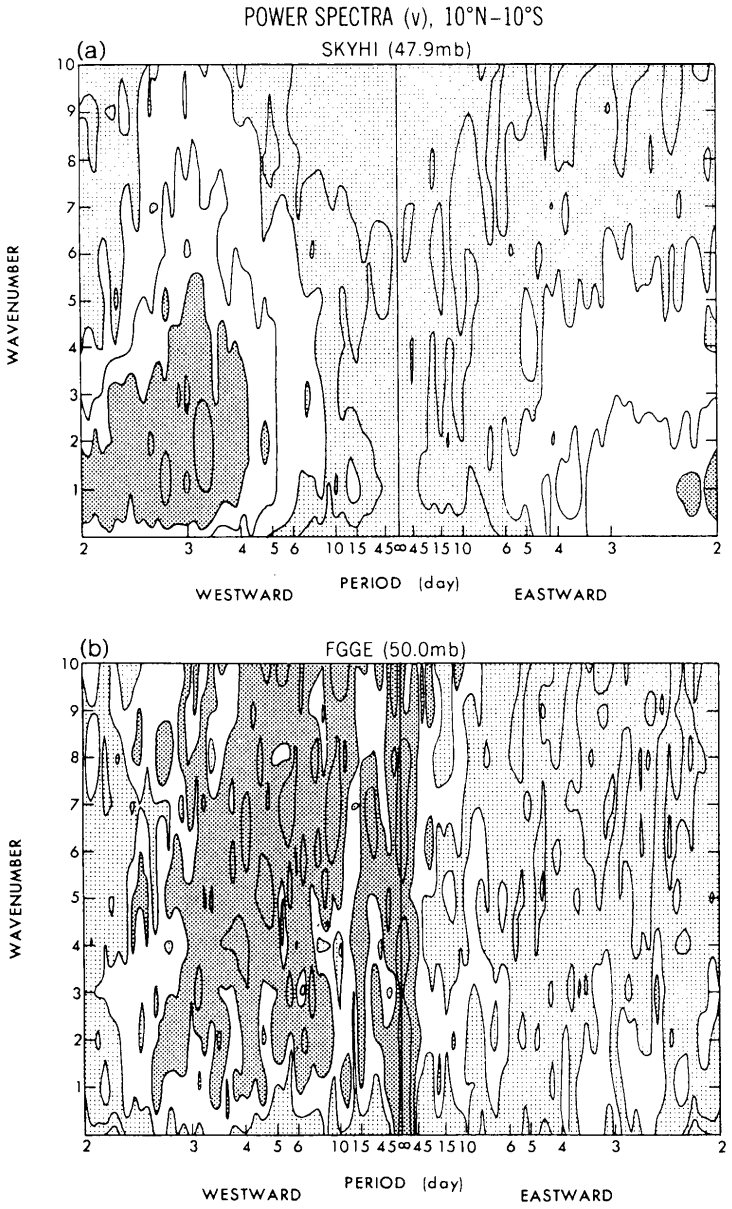

Fig. 15. Wavenumber-frequency distributions of the space-time power spectral density of the meridional velocity averaged over 10°N–10°S for (a) the SKYHI model at 47.9 mb and (b) the FGGE data at 50.0 mb. Contour values: 1, 2, 5, 10, 20, and 50 (0.1 m^2 s^{-2} day). Dark shade > 10, light shade < 5.

waves that have a larger vertical group velocity (see Hayashi 1976, Fig. 5) and a more efficient upward energy propagation than high-wavenumber and low-frequency components. In the corresponding FGGE spectra (Fig. 15b, 50.0 mb), however, the low-wavenumber components are not as pronounced as in the SKYHI spectra. This is probably due to the coarse vertical resolution of the FGGE data. The SKYHI low-wavenumber components are consistent with the upper-stratospheric MRG waves found by Randel *et al.* (1990) in observed satellite temperature data.

At a lower level (781 mb), the SKYHI meridional-wind spectra (Fig. 16a) exhibit a 4–6-day period peak over wavenumbers 2–10, while the FGGE spectra (Fig. 16b, 800 mb) show a somewhat weaker 4–6-day period peak over wavenumbers 4–9. The substantial high-wavenumber components are consistent with lower-tropospheric MRG waves found by Liebmann and Hendon (1990) in the ECMWF data (see also Dunkerton 1993). They are also consistent with the dispersion relation of theoretical MRW waves in the presence of a basic flow. Although the period of the theoretical MRG mode increases with wavenumber in the absence of a basic flow (see Fig. 4), it does not increase for high-wavenumber components in the presence of low-level easterlies, owing to an increase in the westward phase velocity (not

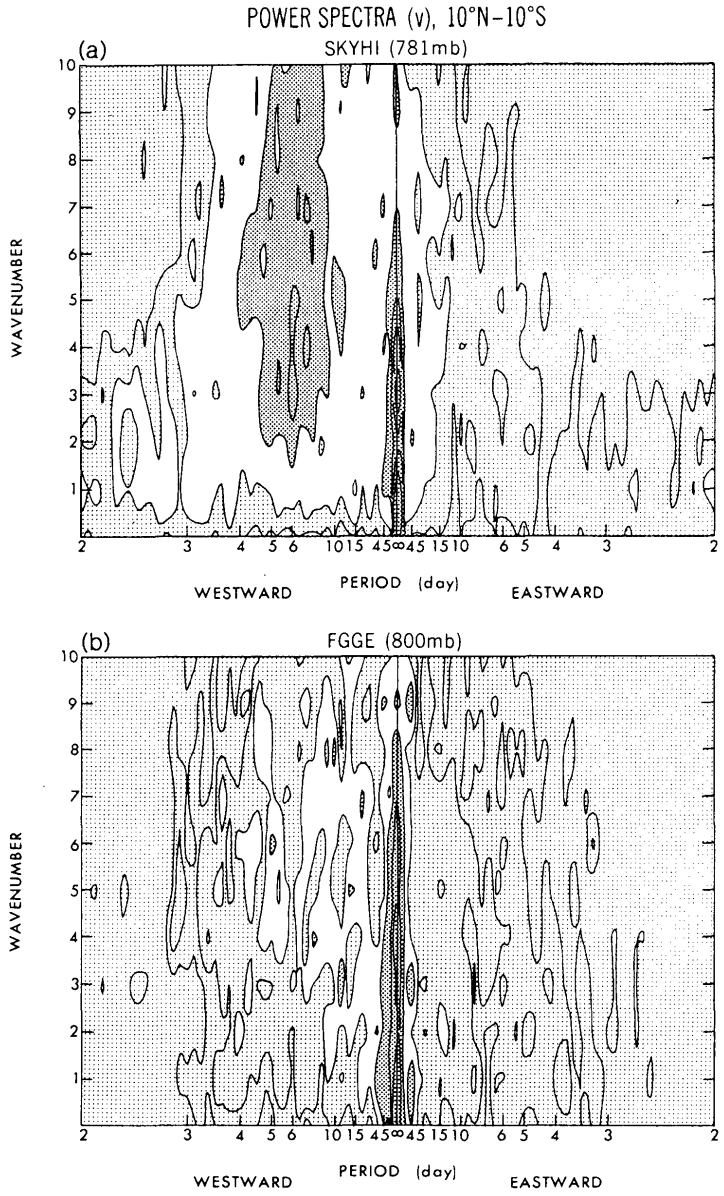

Fig. 16. Wavenumber-frequecny distributions of the spece-time power spectral density of the meridional velocity avereged over 10°N–10°S for (a) the SKYHI model at 781 mb and for (b) the FGGE data at 800 mb. Contour values: 1, 2, 5, 10, 20, 50, and 100 (0.1 m^2 s^{-2} day). Dark shade > 10, light shade < 5.

shown).

Figure 17 compares frequency-height distributions of the power spectral density of wavenumber 3–5 meridional velocities averaged between 10°N–10°S for (a) the SKYHI model and (b) the FGGE data. Only the westward-moving components are shown. Both the SKYHI and FGGE spectra indicate a decrease in the dominant westward-moving periods from the upper troposphere to the stratosphere. This decrease is consistent with the vertical group velocity of MRG waves consisting of different vertical modes, which increases with decreasing period for the same wavenumber. The FGGE spectra above 10 mb are much weaker than the corresponding SKYHI spectra, probably due to the coarse vertical resolution of the FGGE data. The upper-tropospheric spectra are consistent with the low-frequency upper-tropospheric MRG waves found by Randel (1992) in the ECMWF data.

Figure 18 is the same as Fig. 17, except for the wavenumber 1–2 components. As in the wavenumber 3–5 components, the SKYHI and FGGE spectra exhibit a decrease in the dominant westward-moving periods from the upper troposphere to the stratosphere. The FGGE wavenumber 1–2 spectra above 10 mb are much weaker than the correspond-

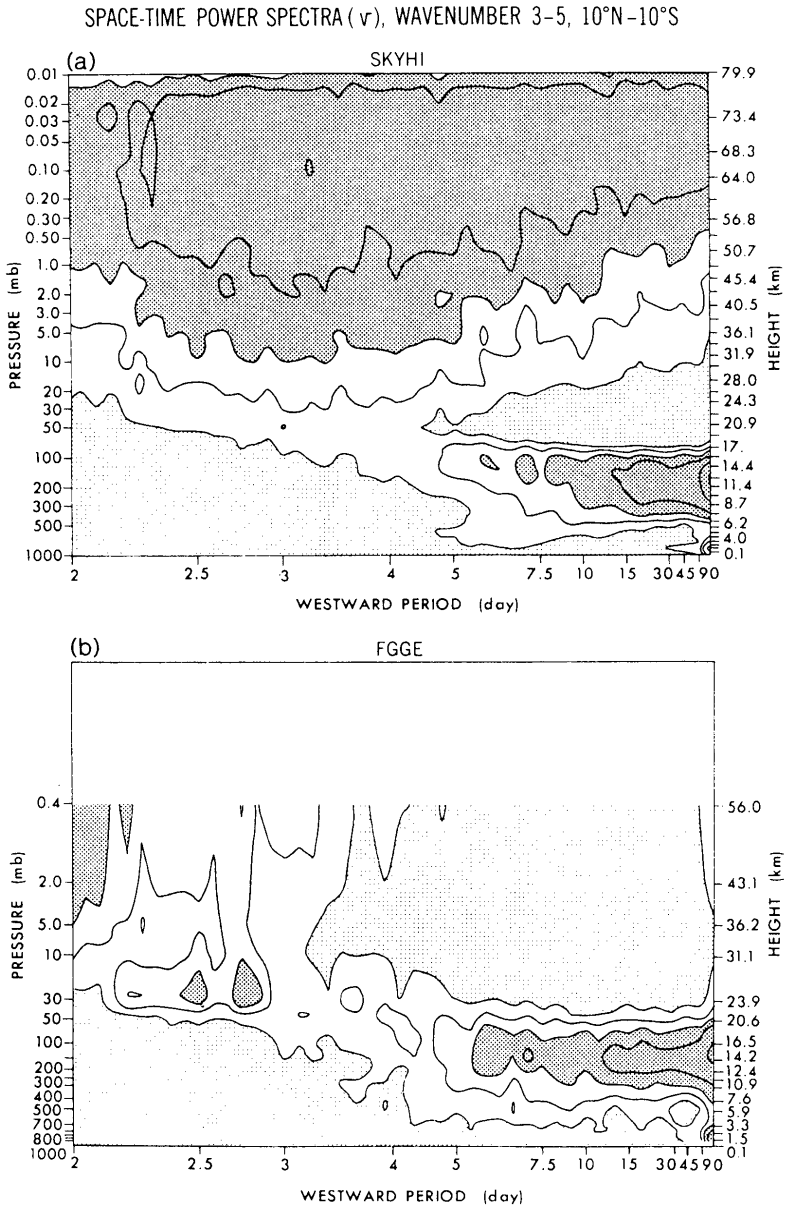

Fig. 17. Frequency-height distributions (wevenumber 3–5) of the space-time power spectral density of the meridional velocity averaged between 10°N–10°S for (a) the SKYHI model and (b) the FGGE data. Only the westward-moving components are shown. Contour values: 2, 5, 10, 20, and 50 (m^2 s^{-2} day). Dark shade > 10, light shade < 2.

ing SKYHI spectra.

To compare the present results with conventional spectral analyses based on station data, Fig. 19 presents the frequency-height distributions of the (a) SKYHI and (b) FGGE time power spectral density (averaged over 150°E–150°W, 5°N–5°S) of the meridional velocity consisting of the wavenumber 0–10 components. For both the SKYHI and FGGE results, the time spectral density values over 4–5-day periods are 20–50 $(m/s)^2$ day. These values are almost the same for each year of the SKYHI data (not illustrated) and are comparable to an observed value (Yanai and Murakami 1970a) based on station data at Canton Island (2°S, 171°W). The amplitude calculated from the time spectral density over the 4–5-day period range is about 2 m/s, which is close to the value quoted for a typical amplitude of observed MRG waves by Wallace (1973). In contrast, for both the SKYHI and FGGE results (Fig. 17a, 17b), the space-time spectral density values over wavenumbers 3–5 and westward-moving periods of 4–5 days in the lower stratosphere are 2–5 $(m/s)^2$ day, being one order of magnitude smaller than the time spectral density. This discrepancy is due to the presence of multiple-wavenumber components (0–10) in the time spectra. The wavenumber-four space-time

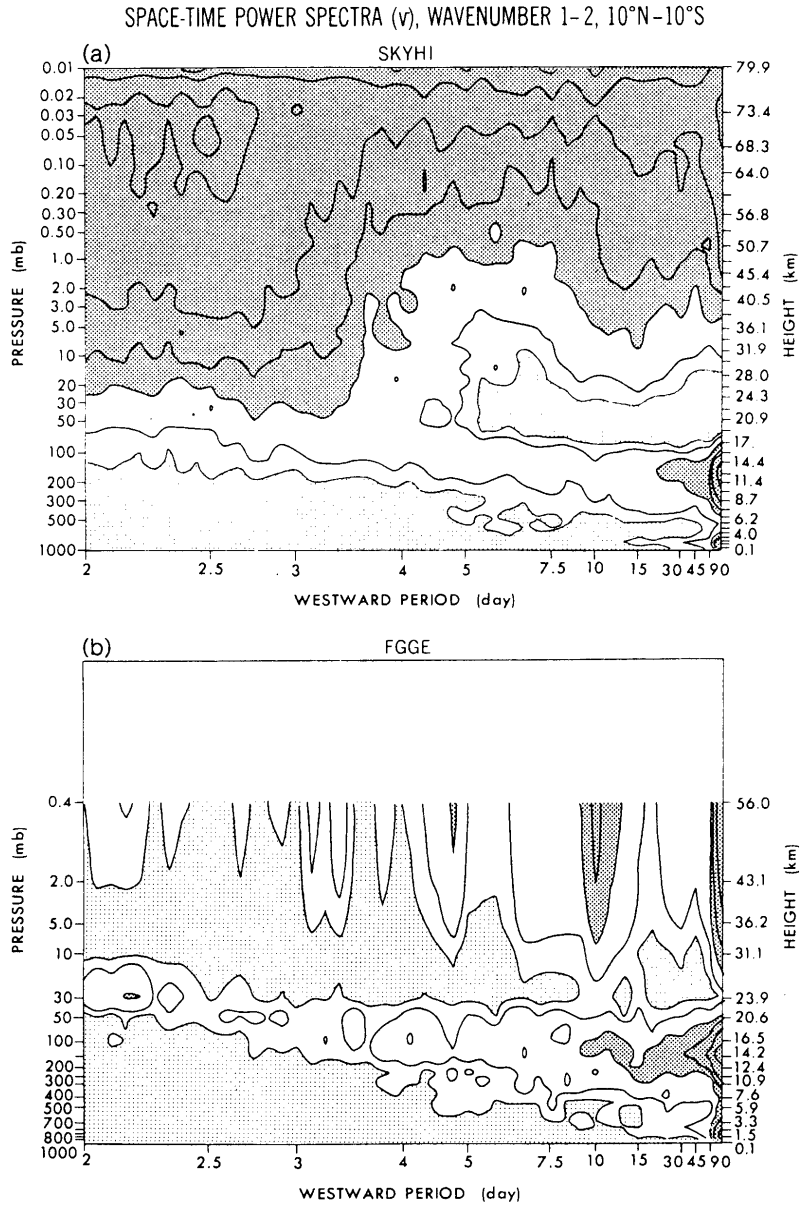

Fig. 18. As in Fig. 17 except for the wavenumber 1–2 components. Contour values: 1, 2, 5, 10, 20, 50, and 100 (m^2 s^{-2} day). Dark shade > 5, light shade < 1.

power spectra appear similar to the time power spectra of the wavenumber-four component (not shown). The multiple-wavenumber components result from the amplitude of MRG waves being localized, as was found in simulated (Hayashi 1974, Fig. 15) and observed (Hendon and Liebmann 1991) MRG waves.

b. Vertical structure

Figure 20a shows the vertical distributions of the space-time amplitude, phase difference, and coherence of the wavenumber four, westward-moving, 5.0-day period component of the meridional velocity averaged between 10°N–10°S for the SKYHI model (solid lines) and the FGGE data (dashed lines). The reference level for the phase difference and coherence is located around 16 km. The SKYHI amplitude has a relative maximum between 10–20 km, exhibits a slight decrease and then increases with height. The SKYHI phaseline tilts westward with height from 15 to 25 km, with a vertical wavelength of 5 km. On the other hand, the FGGE amplitude is largest at 10 km and dereases with height in the stratosphere. The FGGE phaseline does not exhibit a tilt similar to that of the SKYHI phaseline except between 20–25 km. The discrepancies between the SKYHI and FGGE results in the stratosphere are probably due to the coarse vertical resolution of the FGGE data. The westward tilt of MRG waves theoretically implies an upward transport of energy and westerly momentum Lindzen and Matsuno (1968). The lack

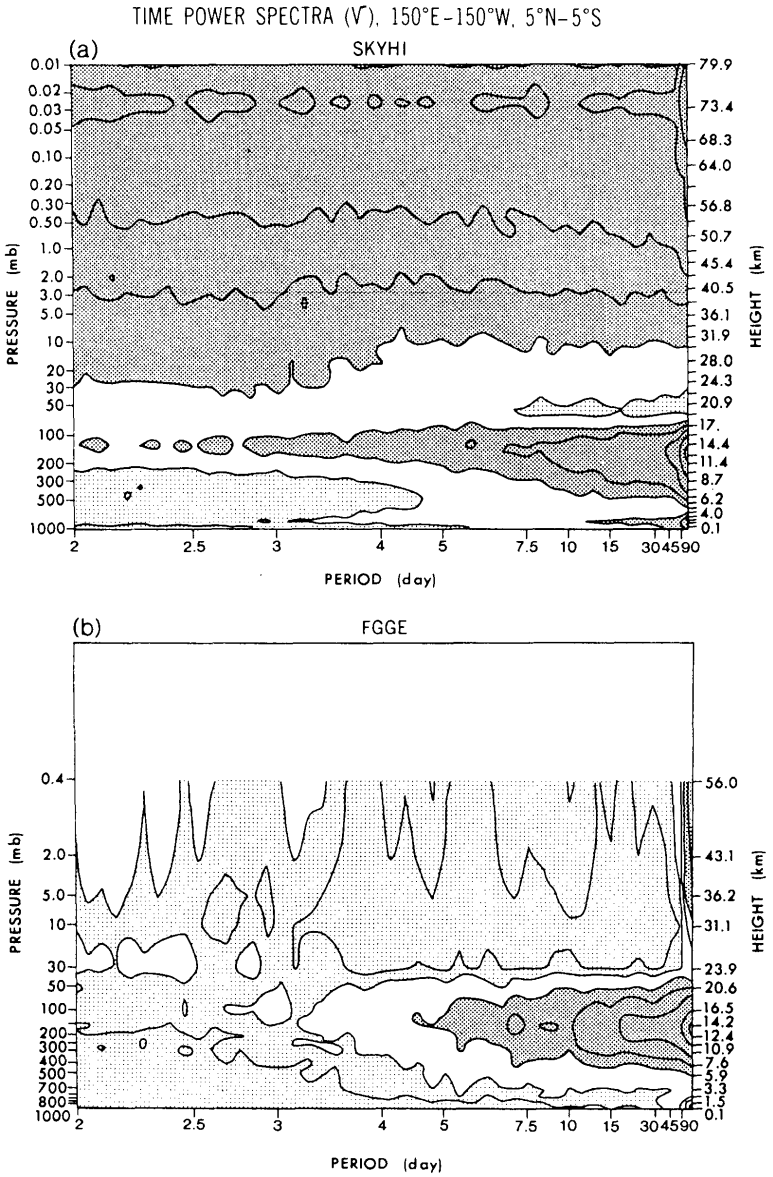

Fig. 19. Frequency-height distributions of (a) the SKYHI and (b) FGGE time power spectral density (averaged over 150°E–150°W, 5°N–5°S) of the meridional velocity consisting of the wavenumber 0–10 components. Contour values: 10, 20, 50, 100, 200, and 500 (m^2 s^{-2} day). Dark shade > 50, light shade < 20.

of vertical tilt and the low value of vertical coherence above 30 km, in both the model and FGGE data, suggest that the upward propagation of the wavenumber-four MRG wave is not very efficient.

Figure 20b is the same as Fig. 20a except for the wavenumber-one, westward-moving 3.0-day-period component, with the reference level located around 21 km. The SKYHI amplitude increases with height from 5 to 40 km, while the FGGE amplitude increases from 0 to 20 km. The SKYHI phaselines tilt westward with height above 15 km, with a typical vertical wavelength of 10 km. In contrast to the wavenumber-four component, this tilt can be detected with high coherence even above 30 km. The FGGE phaseline does not exhibit a similar tilt and is associated with low vertical coherence, probably owing to the coarse vertical resolution of the FGGE data.

c. Horizontal structure

Figure 21 consists of longitude-latitude sections near 50 mb of the wavenumber-one 2–4-day filtered wind vectors and geopotential-height contours of (a) the SKYHI model and (b) the FGGE data. The filtered data have been composited daily during the month of February along the longitude-time isoline of 155 m/s westward phase velocity corresponding to wavenumber one and a period of 3.0 days. Febru-

(a)

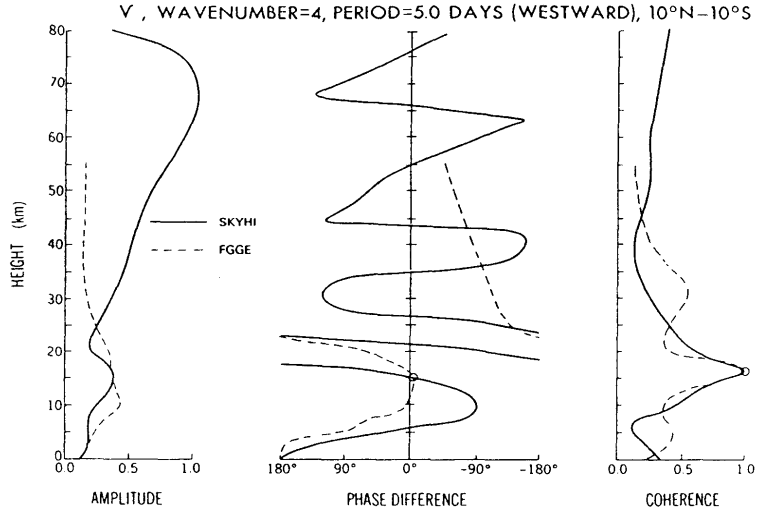

(b)

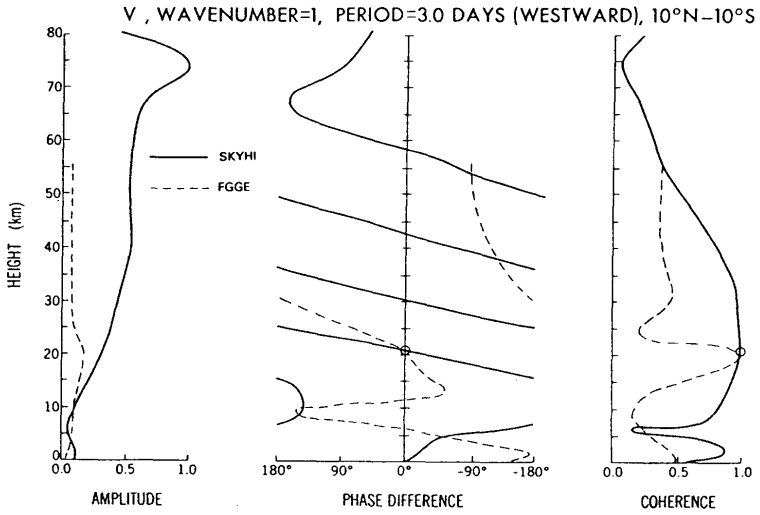

Fig. 20. Vertical distributions of the space-time amplitude (normalized by the maximum SKYHI value), phase difference, and coherence (wavenumber four, period 5.0 days, westward moving) of the meridional velocity averaged between 10°N–10°S for the SKYHI model (solid lines) and the FGGE data (dashed lines). The reference level (16 km) for the phase difference and coherence is indicated by the open circles. (b) As in Fig. 20a except for the wavenumber-one, westward-moving 3.0-day period and reference level at 21 km.

ary was chosen for the compositing presented here, since both the SKYHI and FGGE MRG wave patterns appear very distinctly during this month. In order to enhance the MRG mode, the equatorially symmetric component was extracted for the meridional velocity while the equatorially antisymmetric component was extracted for the zonal velocity and geopotential height (see Yanai and Murakami 1970b for the procedure of the decomposition).

The SKYHI wave pattern between 20°N–20°S resembles the theoretical MRG mode (see Matsuno 1966, Fig. 5b), which is characterized by vortices centered over the equator and a pair of closed contours of high and low geopotential heights straddling the equator. The FGGE pattern exhibits a similar feature except that the MRG wave pattern is confined between 10°N–10°S and that the geopotential height exhibits a considerable meridional tilt. The cause of the discrepancies is not known. The wavenumber-four component with a 4–6-day filter for both the SKYHI and FGGE data also exhibits the MRG mode pattern (not illustrated).

d. Precipitation and evaporation

Figure 22 displays the SKYHI wavenumber-frequency distributions of the equatorially antisymmetric component (see Appendix A) of (a) precipitation and (b) the 537-mb vertical pressure-velocity averaged over 10°N–10°S. Theoretical MRG modes are characterized by symmetric meridional velocity

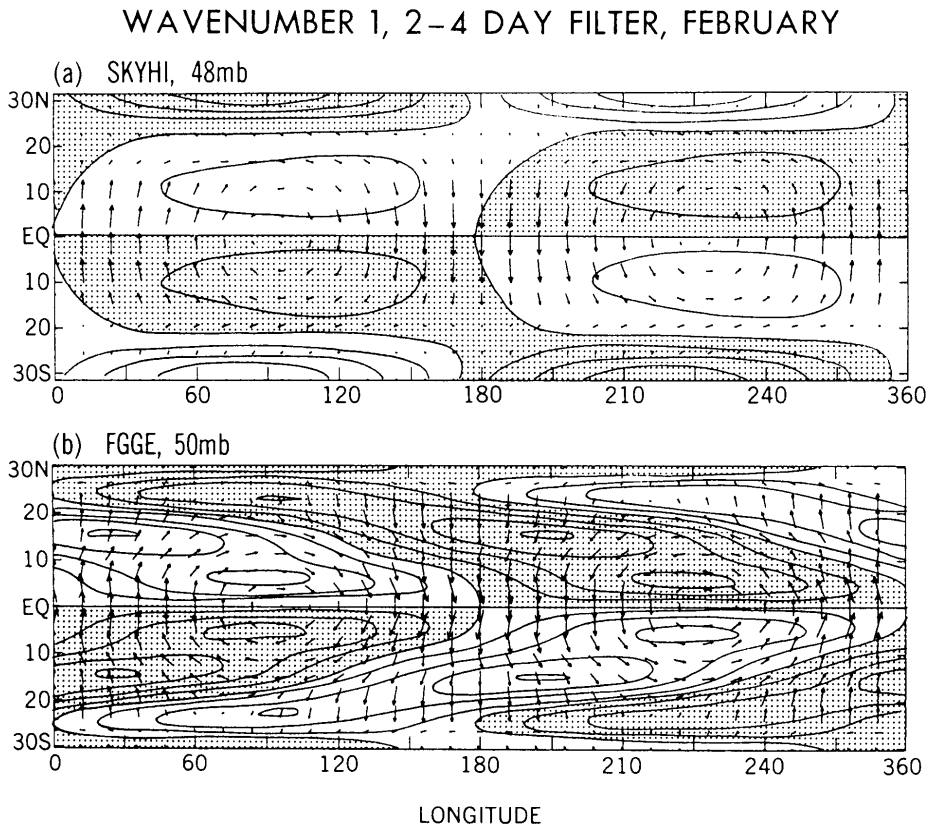

Fig. 21. Longitude-latitude sections of the wavenumber-one component of frequency-filtered wind vectors and geopotential height contours for (a) the SKYHI model at the 48-mb level and (b) the FGGE data at the 50-mb level. The 4–6 day filtered data have been composited over one month (February) along the longitude-time isoline of 155 m/s westward phase velocity. The data have been further modified to extract the equatorially antisymmetric component of the zonal velocity and geopotential and the equatorially symmetric component of the meriodional valocity. Shading indicates positive contour values. The longitudes indicate only relative position. The latitudinal scale and the meridional component have been enlarged by a factor of 2 relative to the longitudinal scale and the zonal component, respectively.

and antisymmetric vertical velocity. As in the symmetric component (Fig. 11), the frequency-spectral distributions are roughly that of red noise; that is, no distinct spectral peak appears, which would correspond to the westward-moving wavenumbers 3–5 and 4–5-day period stratospheric MRG wave. This result is contrary to wave-CISK theory in which both convective heating and vertical velocity have distinct periods. It is also contrary to random thermal-forcing theory, in which the vertical velocity forced by random heating has a distinct periodiciy.

Figure 23 displays the SKYHI wavenumber-frequency distributions (antisymmetric component) of (a) evaporation and (b) the 973-mb zonal velocity averaged over 10°N–10°S. The amplitudes of these variables are confined to lower wavenumbers, in contrast to the precipitation and vertical-velocity amplitudes. Neither the evaporation nor the 973-mb zonal velocity exhibits a distinct spectral peak at westward-moving 4–5-day periods, contrary to an evaporation-wind feedback theory for MRG waves (Goswami and Goswami 1991).

Figure 24a shows the SKYHI vertical distributions (up to 20 km) of the normalized space-time amplitude, phase difference, and coherence (wavenumber four, westward-moving period of 5.0 days) of the equatorially antisymmetric component of vertical pressure-velocity (ω), and convective-adjustment heating (Q) averaged over 10°N–10°S. The phase difference and coherence were measured with reference to $-\omega$ at a height near 5 km. The maximum amplitudes of Q and ω are found in the middle troposphere, contrary to traditional wave-CISK theory in which the heating maximum is prescribed in the upper troposphere to explain the observed 4–5 day MRG waves. When the heating maximum occurs in the middle troposphere, the period of wave-CISK MRG waves should become longer than that observed. The phase difference between Q and $-\omega$ is small, consistent with wave-CISK the-

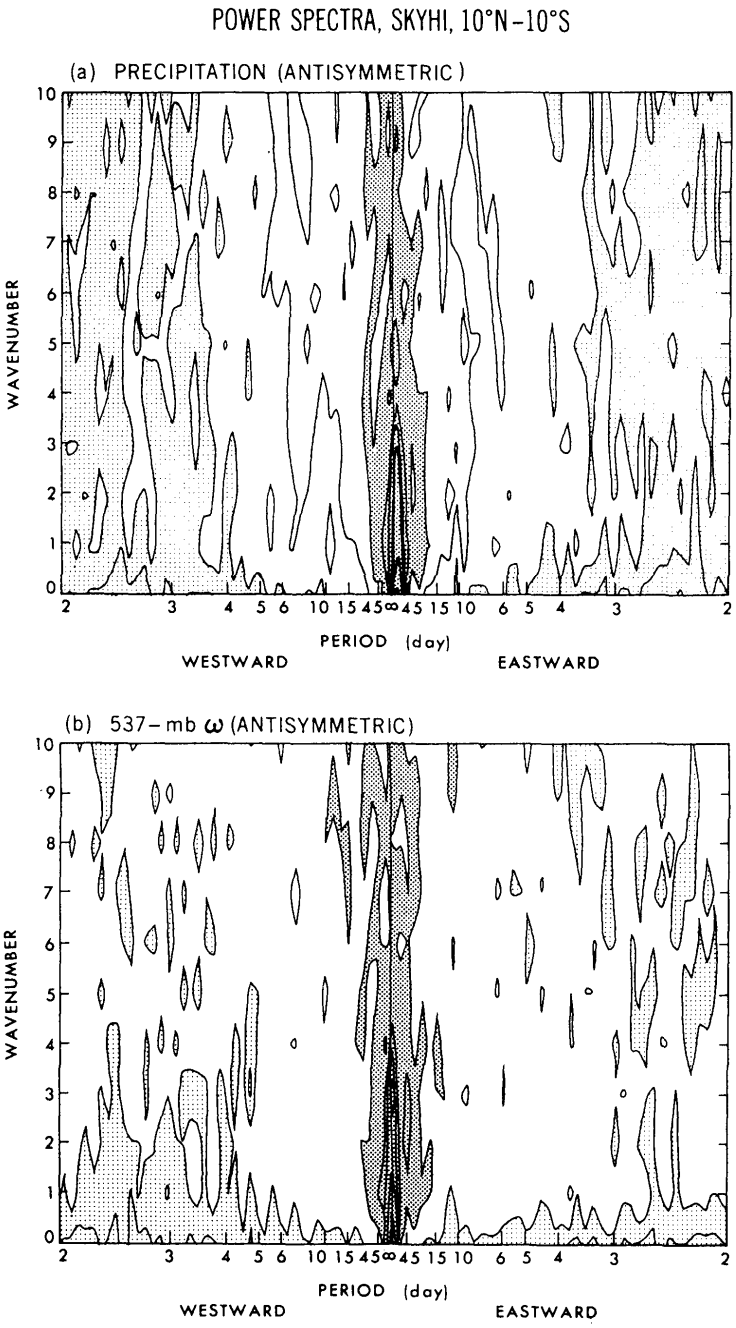

Fig. 22. Wavenumber-frequency distributions of the space-time power spectral density of the antisymmetric component of the SKYHI-model (a) precipitational heating and (b) 537-mb vertical pressure velocity averaged over 10°N–10°S. Contour values for (a): 5, 10, 20, and 50 (23.4 W^2 m^{-4} day); dark shade > 100, light shade < 20. Contour values for (b): 5, 10, 20, 50, 100, 200, and 500 (10 Pa^2 s^{-2} day); dark shade > 50, light shade < 20.

ory, but contrary to random thermal forcing theory which predicts a quadrature-phase relationship. Both Q and ω exhibit a slight eastward tilt in the lower troposphere, with a phase variation of nearly 45 degrees between the 0- and the 5-km level. The eastward tilt of ω can also be found in the FGGE data (Fig. 24b). The eastward tilt of ω is probably due to the effect of boundary-layer convergence and results in a phase lag between the mid-tropospheric convective heating and the low-level convergence. The vertical tilt of Q is contrary to both wave-CISK and random thermal-forcing theories which assume no vertical phase variation in Q.

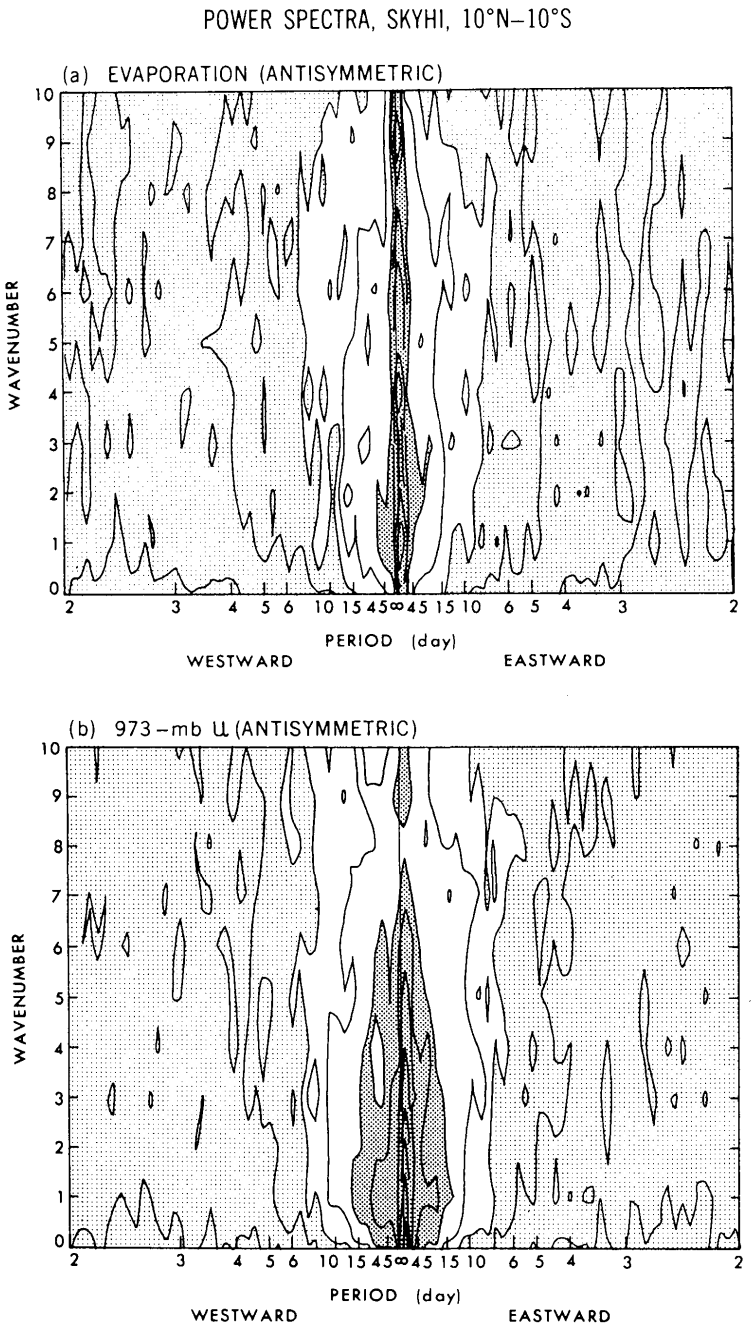

Fig. 23. As in Fig. 22 except for (a) evaporational heating and (b) 973-mb zonal velocity. Contour values for (a): 2, 5, 10, 20, 50, 100, 200, and 500 (2.34 W^2 m^{-4} day); dark shade > 50, light shade < 10. Contour values for (b): 2, 5, 10, 20, 50, 100, 200, 500, and 1000 (0.01 m^2 s^{-2} day); dark shade > 50, light shade < 20.

5. Conclusions and implications

To evaluate simulations and theories of equatorial Kelvin and mixed Rossby-gravity (MRG) waves and to gain insight into their generation mechanism and role in the quasi-biennial oscillation (QBO), space-time spectral analyses were performed on three years of output data from the GFDL "SKYHI" general circulation model and on the GFDL four-dimensional dataset for the FGGE year. The following conclusions have been obtained with respect to the wavenumber-frequency spectral distribution and structure of the waves, and the associated SKYHI precipitation and evaporation:

1) The SKYHI and FGGE Kelvin waves are dominated by an eastward-moving, wavenumber-one, 10–20-day period component in the lower stratosphere. They are accompanied by higher wavenumber-frequency components, which can be

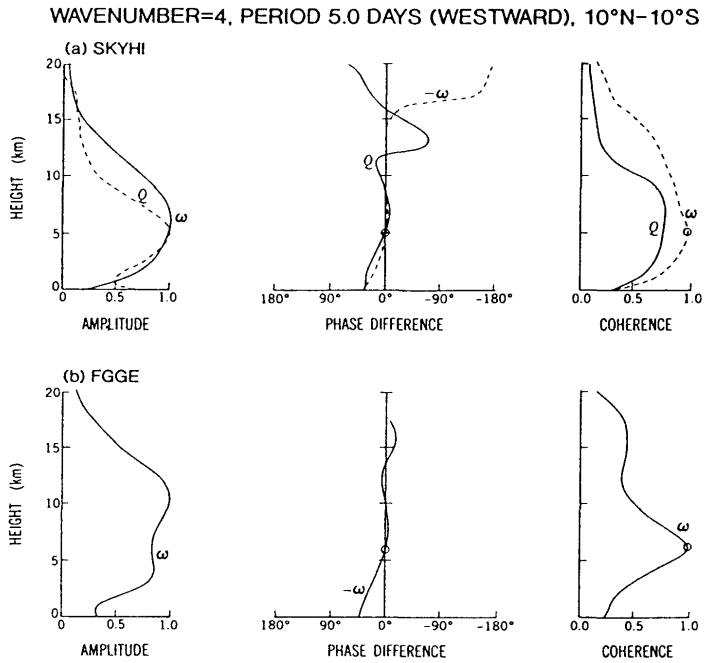

Fig. 24. (a) Vertical distributions of the SKYHI-model normalized space-time amplitude, phase difference, and coherence (wavenumber four, period 5.0 days, westward moving) of the equatorially antisymmetric component of vertical pressure-velocity (ω, solid lines) and convective heating (Q, dashed lines) averaged between 10°N–10°S. The phase difference and coherence are measured with reference to $-\omega$ (open circles) at 537 mb. (b) As in Fig. 24a except for the FGGE data. Convective heating is not available from the FGGE dataset. The phase difference and coherence are measured with reference to $-\omega$ (open cirdes) at 500 mb.

detected more clearly in the upper stratosphere than in the lower stratosphere. This is consistent with the high-frequency Kelvin mode which has a greater vertical group velocity and a more efficient upward energy propagation than the low-frequency Kelvin mode.

2) The SKYHI and FGGE MRG waves are dominated by a westward-moving, wavenumber 3–5, 4–6-day period component in the lower stratosphere, and are dominated by smaller wavenumbers (1–2) and shorter periods (2–4 days) in the upper stratosphere. This is consistent with the high-frequency MRG mode which has a greater vertical group velocity and a more efficient upward energy propagation than the low-frequency MRG mode.

3) The space-time amplitudes of SKYHI Kelvin and MRG waves are comparable to those found in the FGGE data. The time amplitudes of SKYHI/FGGE Kelvin and MRG waves are much greater than the space-time amplitudes and are comparable to time amplitudes estimated from observed (non-FGGE) station data.

4) The SKYHI precipitation and evaporation do not exhibit distinct wavenumber-frequency spectral peaks which would correspond to Kelvin and MRG waves, being consistent with random thermal-forcing theory, but contrary to wave-CISK and evaporation-wind feedback theories. The SKYHI tropospheric convective heating and vertical velocity corresponding to Kelvin and MRG wavenumber-periods are nearly in phase, being consistent with wave-CISK and evaporation-wind feedback theories, but contrary to random-forcing theory.

On the basis of the above results, the authors propose a unified wave-generation mechanism which combines instability and random-forcing theories. This mechanism consists of the following processes:
1) Kelvin, MRG, and gravity waves are weakly unstable waves, while tropical intraseasonal oscillations are strongly unstable waves. These unstable waves result from the coupling between waves and convection.
2) Kelvin, MRG, and gravity waves are intermittently triggered by random convective heating, while tropical intraseasonal oscillations grow essentially through evaporation-wind feedback instability.
3) MRG and gravity waves can also be triggered by extratropical disturbances.

In the present model, moist convective adjustment could couple waves and convection through "prognostic" adjustment which continually adjusts temperature and moisture changes primarily due to adiabatic cooling, moisture convergence, and evaporation. On the other hand, moist convec-

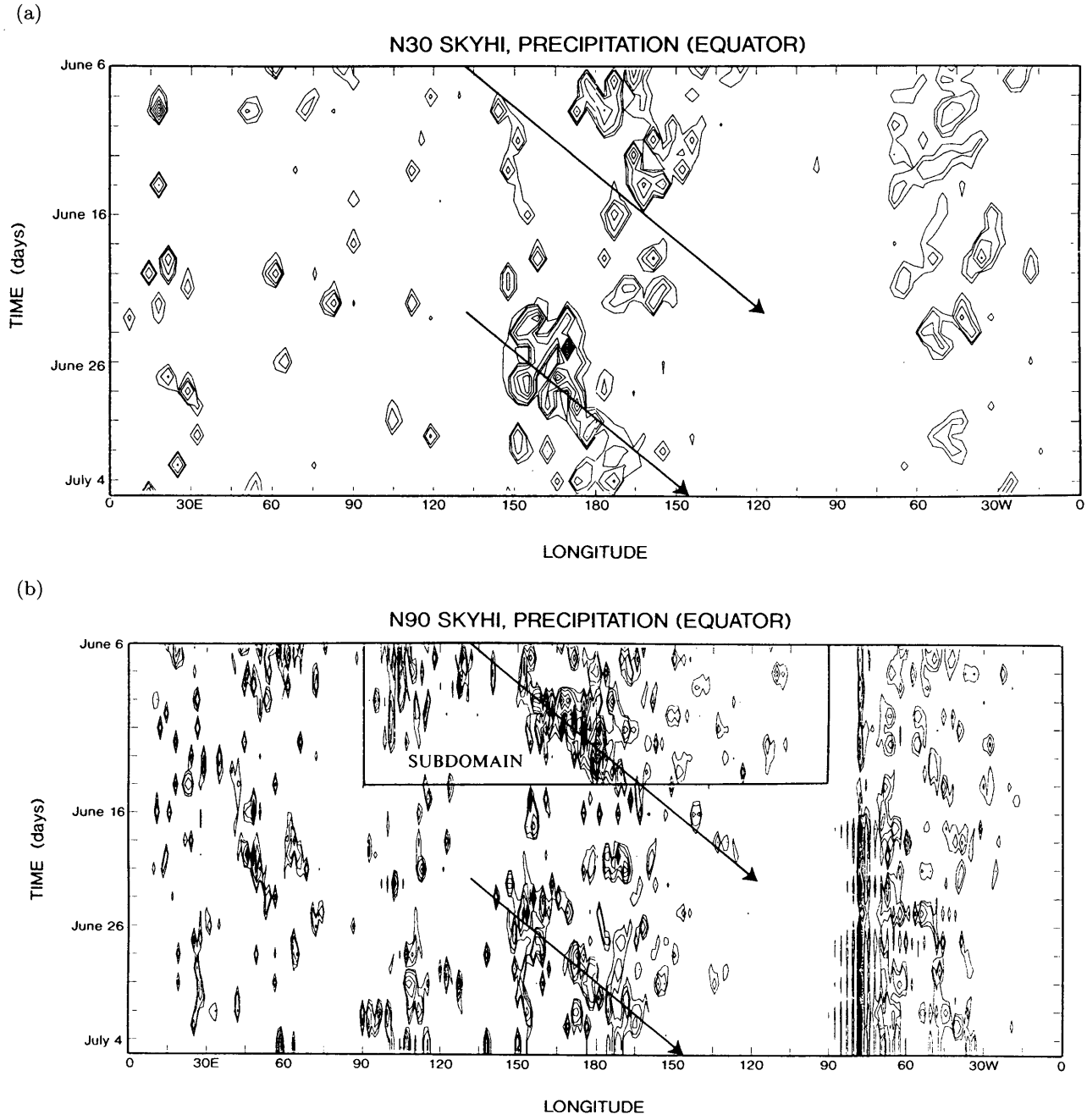

Fig. 25. Longitude-time distributions of the daily accumulated precipitational heating at the equator, simulated by (a) N30 and (b) N90 SKYHI models. Contour values: 0.5, 1, 2, 4, 6, 8, 10, and 12 (485 W m^{-2}).

tive adjustment could also trigger random pulses of convective heating through "diagnostic" adjustment which abruptly neutralizes, upon intermittent supersaturation, any pre-existing conditionally unstable stratification (*i.e.*, the "saturation-triggering mechanism"). Random thermal-forcing theories lack the coupling between waves and convection, while instability theories lack the triggering process. The proposed mechanism is currently being investigated both numerically and theoretically.

To gain an insight into the heating due to convective adjustment, Fig. 25 shows longitude-time distributions of the daily accumulated precipitation at the equator during June, simulated by the (a) N30 and (b) N90 SKYHI models with 3° × 3.6° and 1 × 1.2 latitude-longitude resolutions, respectively. It can be seen that grid-size pulses of precipitation appear intermittently. These pulses are triggered through diagnostic adjustment and magnified through prognostic adjustment. The width of the N90 pulses is smaller than that of the N30 pulses, while the intensity, density, and frequency of the N90 pulses

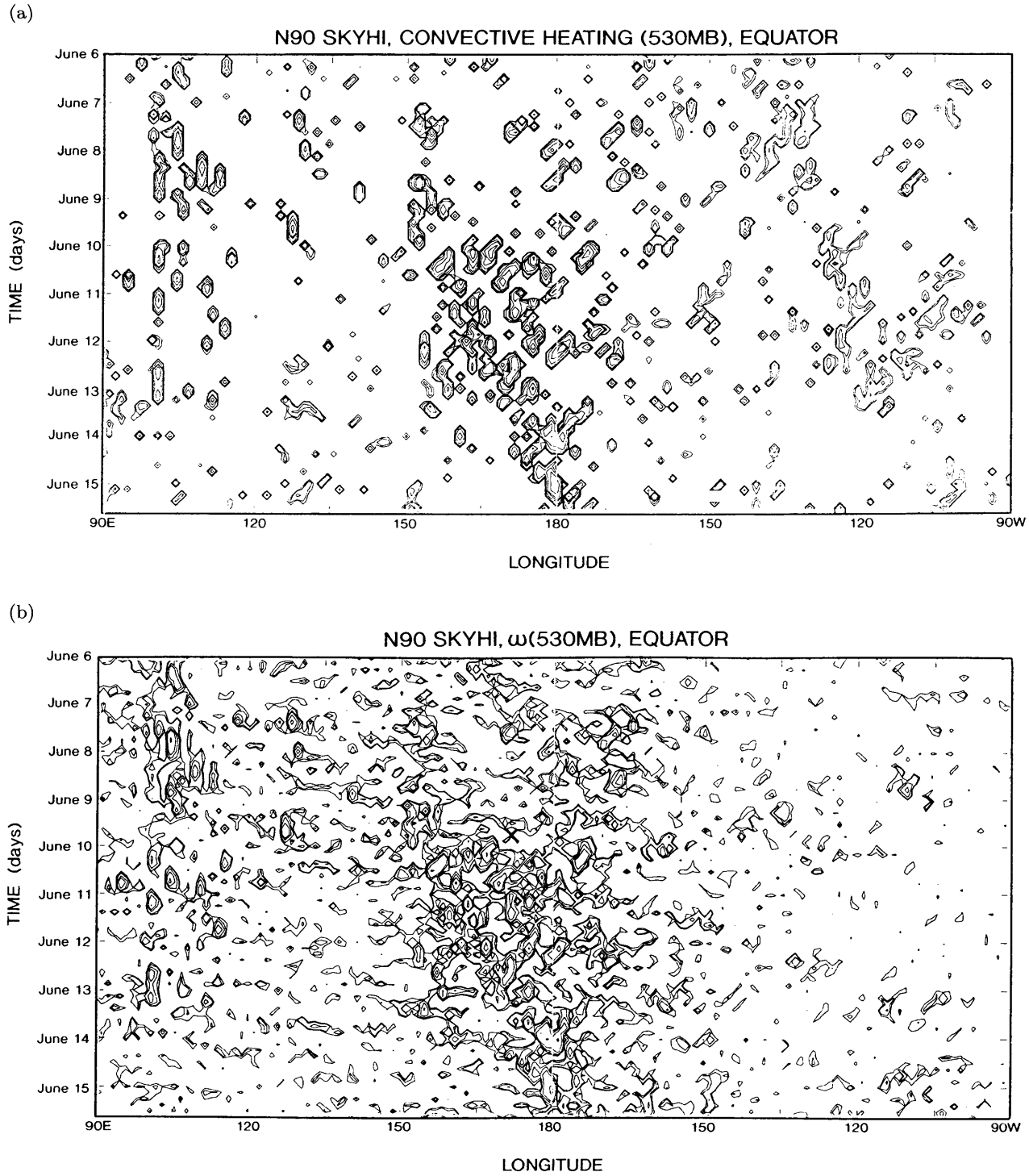

Fig. 26. (a) Longitude-time distribution at the equator of N90 convective heating sampled every three hours at the 530-mb level over the limited longitiude-time span (90°E to 90°W and the period June 6–16), which is the rectangular subdomain displayed in Fig. 25b. Contour values 0.01, 0.02, 0.05, 0.1, 0.2, 0.5, 1, 2, 5, and 10 (100 K/day). (b) As in Fig. 26a except for 530-mb vertical pressure-velocity (contours are drawn only for upward velocity). Contour values 0.1, 0.2, 0.5, 1, 2, 5, and 10 (mb/s). (c) As in Fig. 26b except for the 102-mb vertical pressure-velocity (contours are drawn only for upward velocity). Contours 0.1, 0.2, 0.5, 1, 2, 5, and 10 (0.1 mb/s).

(c)

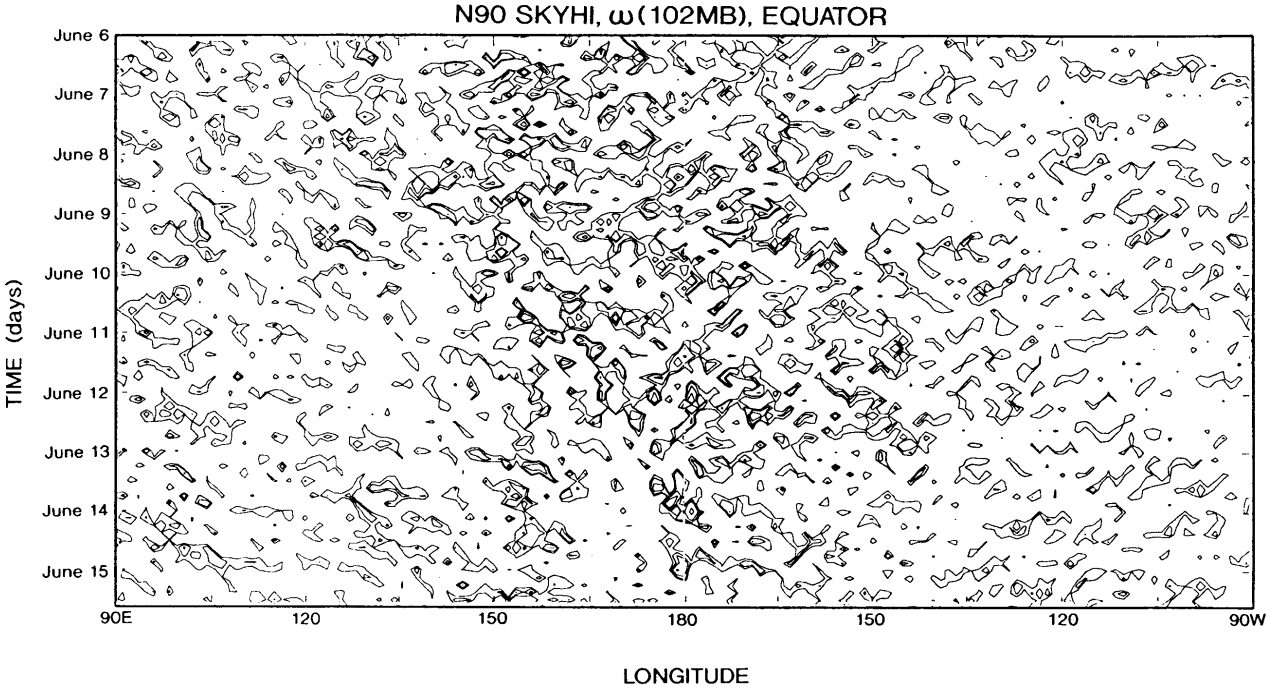

Fig. 26. (Continued)

are greater than those of the N30 pulses. As indicated by arrows, groups of these pulses exhibit a slow (5–10 m/s) eastward propagation, corresponding to observed superclusters having a half wavelength of 2000–4000 km (Nakazawa 1988; Hayashi and Nakazawa 1989).

To examine the pulses of convective heating in more detail, Fig. 26a shows the longitude-time distribution of the N90 SKYHI equatorial convective heating at 530 mb over the limited longitude-time span (90°E to 90°W, and the period June 6–16), which corresponds to the rectangular subdomain displayed in Fig. 25b. The individual pulses appear to propagate westward rather than eastward around the 180° longitude, where the superclusters are seen to propagate eastward. However, these pulses appear stationary around 100°E, where the eastward-moving superclusters are not clearly seen. These pulses could crudely represent mesoscale (100 km) cloud clusters which are observed (Nakazawa 1988) to propagate westward. Recently, Takayabu (1994a, b) suggested observationally that westward-moving cloud clusters are due to westward-moving gravity waves.

Figure 26b is the same as Fig. 26a except for the vertical pressure velocity (contours are drawn only for upward velocity). The 530-mb vertical velocity has a major supercluster component consisting of grid-size pulses of upward vertical velocity. In addition, the vertical velocity has a minor gravity-wave component consisting of both upward (shown) and downward (not shown) velocites. These gravity waves are composed of both eastward- and westward-moving components, which are probably triggered by the convective-heating pulses. Figure 26c is the same as Fig. 26b except for the 102-mb level. In contrast to the 530-mb level, the 102-mb vertical velocity has a major gravity-wave component, indicating that this component propagates upward more efficiently than the supercluster-scale component.

The present study has demonstrated that the Kelvin and MRG waves simulated by the SKYHI model have realistic amplitudes, while the N30 SKYHI model simulates an unrealistically weak stratospheric QBO (Hamilton *et al.*, 1994), the amplitude being about 10 % of the observed value (20–30 m/s). A realistic QBO is not simulated, however, even with greatly enhanced vertical resolution and a more accurate vertical convergence of eddy momentum flux (Hamilton and Yuan 1992). According to the results of a three-dimensional mechanistic model (Takahashi and Boville 1992), the amplitudes of Kelvin and MRG waves must be unrealistically large in order for the model to adequately produce the QBO.

In view of the above difficulties, the authors speculate that the QBO is primarily produced by gravity waves which are intermittently triggered by random pulses of convective heating. Small-scale gravity waves and grid-size convective heating are probable not adequately produced by the present SKYHI model, owing to the insufficient horizontal resolution of the model.

According to Hayashi *et al.* (1989), the tropical gravity-wave momentum flux increased by a factor of two, when the horizontal resolution of the SKYHI model was increased from N30 to N90. In contrast, the tropical gravity-wave kinetic energy did not increase with horizontal resolution. This is probably due to the effect of the earth's rotation on the partition between the rotational and divergent winds of rotational gravity waves. In contrast to the gravity-wave momentum flux, the kinetic energy of gravity waves simulated by the N30 SKYHI model is comparable to that found in observed tropical and extratropical station data (Hamilton 1993).

It has been observationally suggested (Carter and Balsley 1982; Fritts 1984) that the kinetic energy spectra of simulated gravity waves follow an approximate $-5/3$ distribution over frequencies greater than 1/day. The N90 SKYHI model exhibits such an approximate $-5/3$ distribution of kinetic energy over wavenumbers greater than around 50 (see Hamilton 1993, Fig. 5). The lower limit for the horizontal wavelength of theoretical internal gravity waves with a phase speed of 30 m/s is about 10 km (see Jones 1969). This wavelength corresponds to wavenumber 4000 which could be resolved by an N2400 resolution model. Theoretically, the $-5/3$ distribution in the kinetic energy of gravity waves corresponds to a $-2/3$ distribution in the vertical momentum flux (see Hamilton 1993, p. 170).

When the kinetic energy is assumed to be constant over wavenumbers 1–50 and then decreases with a $-5/3$ distribution, the energy is expected to increase by a factor of only 2.5 from N30 to N2400, 2.4 from N30 to N900, and 1.8 from N30 to N90. In contrast, when vertical momentum flux is assumed to be constant over wavenumber 1–50 and then decreases with a $-2/3$ distribution, the flux is expected to increase by a factor of as much as 11 from N30 to N2400, 7.5 from N30 to N900, and 2.4 from N30 to N90. It is unknown whether the QBO amplitude will increase by a factor of nearly two when the model resolution is increased from N30 to N90, since the N90 model has not been integrated for a sufficiently long period. The expected increase should be examined by extending the integration of the N90 model in order to test the hypothesis that gravity waves primarily force the QBO.

The SKYHI model also simulates a realistic stratopause semiannual oscillation (SAO) and an unrealistically weak mesopause SAO (Mahlman and Umscheid 1984). The westerly phase of the SAO simulated by the SKYHI model is primarily produced by the vertical momentum flux associated with gravity waves explicitly simulated by the model (Hamilton and Mahlman 1988). This result is consistent with the observed estimate (Hitchman and Leovy 1988) of the mean flow forcing due to Kelvin waves, which is too weak to account for the SAO. On the other hand, the NCAR community model (CCM2) simulates an SAO having unrealistically weak westerlies (Sassi *et al.*, 1993). This deficiency is probably due to the fact that the gravity waves simulated in the CCM2 model are much weaker than the simulated Kelvin waves. The weak gravity-wave amplitudes may be due to the absence of the "above-proposed" saturation-triggering mechanism in the simple mass-flux convective parameterization employed in the CCM2 model.

The realistic amplitude of the SKYHI stratopause SAO in spite of presumably weak gravity waves is probably due to the following mechanisms. First, the phase speed of the gravity waves that produce the SKYHI SAO is about 55 m/s (Hamilton and Mahlman 1988), being faster than that (30 m/s) of the gravity waves which would produce the QBO. Fast gravity waves have a fast vertical group velocity and their vertical momentum flux decays slowly with height, thereby penetrating through the stratopause. Since the zonal momentum is much weaker in the mesosphere than in the stratosphere due to the lesser density, a weak momentum convergence is sufficient to produce a strong SAO. Second, high-wavenumber fast gravity waves, which presumably exist in the real atmosphere, do not efficiently deposit momentum to contribute to the stratopause SAO, since the vertical group velocity of fast gravity waves increases with horizontal wavenumber.

The weakness of the SKYHI mesopause SAO may be due to the absence of the high-wavenumber components of fast gravity waves, which propagate more efficiently to the mesopause than the low-wavenumber components. The weakness may also be due to the effect of the upper boundary condition imposed near the mesopause (see Hamilton and Mahlman 1988 for a discussion of several other possible causes).

The weakness of the SKYHI QBO may be due to the absence of the high-wavenumber components of slow gravity waves. In contrast to fast gravity waves, the vertical group velocity of slow gravity waves may not substantially increase with horizontal wavenumber. This is because the vertical group velocity of gravty waves is not only proportional to the horizontal wavenumber, but also to the relative phase velocity $(c - U)$ squared (Appendix A, Eq. A3a), which vanishes at the critical level. Thus, even for high wavenumbers, slow gravity waves can efficiently deposit momentum near the critical level in the lower stratosphere to produce a strong QBO.

The effect of gravity waves, in addition to fast Kelvin waves, was incorporated in several mechanistic models of the SAO (*e.g.*, Dunkerton 1982; Takahashi 1984). However, the gravity waves were represented by a single-wavenumber component which is comparable to or even weaker than the fast Kelvin waves. The mechanistic models should be modified

in such a way that both the QBO and SAO are produced by multiple-wavenumber gravity waves, even without the inclusion of Kelvin and MRG waves.

Recently, Held *et al.* (1993) demonstrated that a strong "QBO-like" oscillation with a period of about 60 days is produced by gravity waves generated in a two-dimensional idealized model with an explicit scheme of moist convection. On the other hand, Takahashi (1993), and Takahashi and Shiobara (1994) demonstrated that strong "QBO-like" oscillations with periods of about 60 days and 400 days are produced in two- and three-dimensional idealized models, respectively, by gravity waves generated in the presence of moist convective adjustment. In the realistic SKYHI model, however, such unrealistic "QBO-like" oscillations are somehow prevented from occurring, while a weak QBO emerges.

Acknowledgments

The authors are grateful to Drs. J.D. Mahlman and S. Manabe for their valuable advice and to Drs. K. Hamilton and I.M. Held for their appropriate comments on the original manuscript.

Appendix

A : *Vertical group velocity*

The dispersion relation for Kelvin waves and two-dimensional irrotational internal gravity waves in an isothermal atmosphere with a constant basic flow is given by

$$(6 - kU) * *2 = (N * *2\ k * *2) \\ / \ (m * *2 + k * *2 + s * *2), \quad \text{(A1a)}$$

or equivalently

$$m * *2 = [N * *2/(c-U) * *2] - k * *2 - s * *2. \quad \text{(A1b)}$$

Here 6 is the wave frequency, while k and m are the zonal and vertical wavenumbers, respectively. N is the buoyancy frequency, while s is defined as $1/(2H)$ where H is the scale height. U is the constant basic flow, while c is the absolute phase velocity given by $6/k$.

The vertical group velocity C_g is derived (*e.g.*, see Hayashi 1976) by taking the derivative of 6 with respect to m as

$$C_g = Nkm \\ / \ [(m * *2 + k * *2 + s * *2) * *(3/2)], \quad \text{(A2a)}$$

$$= [k(c - U) * *3/N * *2][N * *2/(c - U) * *2 \\ - k * *2 - s * *2] * *(1/2), \quad \text{(A2b)}$$

where (A1a) and (A1b) have been used to derive (A2b) from (A2a).

The C_g determined by (A2b) is graphically illustrated as a function of k, 6, and $c-U$ in Jones (1969, Fig. 1)

For either small relative phase velocity $(c - U)$ or small values of k and s, (A2b) can be approximated as

$$C_g = k(c - U) * *2/N * *2, \quad \text{(A3a)}$$

$$= (6 - kU)(c - U)/N * *2, \quad \text{(A3b)}$$

$$= [(6 - kU) * *2/k]/N * *2. \quad \text{(A3c)}$$

B : *Time spectra of multi-wavenumber components*

This appendix proves that even when the space-time power spectrum of minor wavenumber components is negligible compared with that of the major wavenumber component, the time power spectra of the multiple-wavenumber components can be much larger than that of the major wavenumber component.

As a simple example, the space-time series $W(x,t)$ is assumed to consist of two traveling wave components having the same frequency 6 and two different wavenumbers $k1$ and $k2$ as

$$W = A1\cos(k1x + 6t) + A2\cos(k2x + 6t). \quad \text{(B1)}$$

The space-time power spectra $P1$ and $P2$ of these components can be calculated as the space-time variance of each component, resulting in

$$P1 = A1 * *2/2, \quad \text{(B2)}$$

and

$$P2 = A2 * *2/2. \quad \text{(B3)}$$

On the other hand, the time power spectrum P of the series W can be calculated as the time variance of the sum of the two components, resulting in a function of x as

$$P = (A1 * *2 + A2 * *2)/2 + A1A2\cos(k1 - k2)x, \quad \text{(B4)}$$

with its maximum and minimum values $Pmax$ and $Pmin$ given by

$$Pmax = (A1 + A2) * *2/2, \quad \text{(B5)}$$

and

$$Pmin = (A1 - A2) * *2/2. \quad \text{(B6)}$$

When the space-time ampltudes are $A1 = 1.0$ and $A2 = 0.4$, the respective space-time power spectra have values of $P1 = 0.5$ and $P2 = 0.08$, the ratio being $P2/P1 = 0.16$. This means that the space-time power spectrum of the minor component is negligible compared with that of the major component. On the other hand, the maximum value ($Pmax$) of the time power spectra is 0.98, the ratio ($Pmax/P1$) being equal to 1.96. This means that the time power spectrum ($Pmax$) consisting of the two components can be twice as large as the space-time power spectrum ($P1$) of the major component,

whereas the time spectrum of the major component alone equals the space-time power spectrum. The ratio between the time power spectrum of the sum of all components and the space-time power spectrum of the major component increases as the number of minor components increases.

References

Andrews, D.G. and M.E. McIntyre, 1976: Planetary waves in horizontal and vertical shear: Asymptotic theory for equatorial waves in weak shear: The generalized Eliassen-Palm relation and the mean zonal acceleration. *J. Atmos. Sci.*, **33**, 2031–2048.

Andrews, D.G., J.D. Mahlman and R.W. Sinclair, 1983: Eliassen-Palm diagnostics of wave-mean flow interaction in the GFDL "SKYHI" general circulation model. *J. Atmos. Sci.*, **40**, 2768–2784.

Boville, B.A. and W.J. Randel, 1992: Equatorial waves in a stratospheric GCM: Effects of vertical resolution. *J. Atmos. Sci.*, **49**, 785–801.

Cariolle D., M. Amodei, M. Deque, J.-F. Mahfouf, P. Simon and H. Teyssedre, 1993: A quasi-biennial oscillation signal in general circulation simulations. *Science*, **261**, 1313–1316.

Carter, D.A. and B.B. Balsly, 1982: The summer wind field between 80 and 93 km observed by the MST radar at Poker Flat, Alaska (65N). *J. Atmos. Sci.*, **39**, 2905–2915.

Chang, C.-P., 1976: Forcing of stratospheric Kelvin waves by tropospheric heat sources. *J. Atmos. Sci.*, **33**, 740–744.

Dunkerton, T.J., 1982: Theory of mesopause semiannual oscillation. *J. Atmos. Sci.*, **39**, 2681–2690.

Dunkerton, T.J., 1993: Observation of 3–6-day meridional wind oscillations over the tropical Pacific, 1973–1992: Vertical structure and interannual variability. *J. Atmos. Sci.*, **50**, 3292–3307.

Emanuel, K.A., 1987: An air-sea interaction model of intraseasonal oscillations in the tropics. *J. Atmos. Sci.*, **44**, 2324–2340.

Fels, S.B., J.D. Mahlman, M.D. Schwarzkopf, and R.W. Sinclair, 1980: Stratospheric sensitivity to perturbations in ozone and carbon dioxide: Radiation and dynamical response. *J. Atmos. Sci.*, **37**, 2265–2297.

Fritts, D.C., 1984: Gravity wave saturation in the middle atmosphere: A review of theory and observations. *Rev. Geophys. Space Phys*, **22**, 275–308.

Garcia, R.R. and M.L. Salby, 1987: Transient response to localized episodic heating in the tropics Part II: Far-field behavior. *J. Atmos. Sci.*, **44**, 499–530.

Goswami, P. and B.N. Goswami, 1991: Modification of $n = 0$ equatorial waves due to interaction between convection and dynamics. *J. Atmos. Sci.*, **48**, 2231–2244.

Hamilton, K., 1993: What we can learn from the general circulation models about the spectrum of middle atmospheric motions. *Coupling Processes in the Lower and Middle Atmosphere*, Kluwer Academic Publishers, Netherlands, 161–174.

Hamilton, K. and J.D. Mahlman, 1988: General circulation model simulation of the tropical middle atmosphere. *J. Atmos.*, **45**, 3212–3235.

Hamilton, K. and L. Yuan, 1992: Experiments on tropical stratospheric mean-wind variations in a spectral general circulation model. *J. Atmos. Sic.*, **49**, 2464–2483.

Hamilton, K., R.J. Wilson, J.D. Mahlman and L.J. Umscheid, 1994: Climatology of the SKYHI troposphere-stratosphere-mesosphere general circulation model. Submitted to *J. Atmos. Sci.*

Hartmann, D.L., M.L. Michelsen and S.A. Klein, 1992: Seasonal variations of tropical intraseasonal oscillations: A 20–25 day oscillation in the western Pacific. *J. Atmos. Sci.*, **49**, 1277–1289.

Hayashi, Y., 1970: A theory of large-scale equatorial waves generated by condensation heat and accelerating the zonal wind. *J. Meteor. Soc. Japan.*

Hayashi, Y., 1974: Spectral analysis of tropical disturbances appearing in a GFDL general circulation model. *J. Atmos. Sci.*, **31**, 180–218.

Hayashi, Y., 1976: Non-singular resonance of equatorial waves under the radiation condition. *J. Atmos. Sci.*, **33**, 183–201.

Hayashi, Y., 1982: Space-time spectral analysis and its applications to atmospheric waves. *J. Meteor. Soc. Japan*, **60**, 156–171.

Hayashi, Y. and D.G. Golder, 1978: The generation of equatorial transient planetary waves: Control experiments with a GFDL general circulation model. *J. Atmos. Sci.*, **35**, 2068–2082.

Hayashi, Y. and D.G. Golder, 1980: The seasonal variation of tropical transient planetary waves appearing in a GFDL general circulation model. *J. Atmos. Sci.*, **37**, 705–716.

Hayashi, Y. and D.G. Golder, 1986: Tropical intraseasonal oscillations appearing in a GFDL general circulation model and FGGE data. Part I: Phase propagation. *J. Atmos. Sci.*, **43**, 3058–3067.

Hayashi, Y. and D.G. Golder, 1988: Tropical intraseasonal oscillations appearing in a GFDL general circulation model and FGGE data. Part II: Structure. *J. Atmos. Sci.*, **45**, 3017–3033.

Hayashi, Y. and D.G. Golder, 1993: Tropical 40–50- and 25–30-day oscillations appearing in realistic and idealized GFDL-climate models and the ECMWF dataset. *J. Atmos. Sci.*, **50**, 464–494.

Hayashi, Y., D.G. Golder and J.D. Mahlman, 1984: Stratospheric and mesospheric Kelvin waves simulated by the GFDL "SKYHI" general circulation model. *J. Atmos. Sci.*, **41**, 1971–1984.

Hayashi, Y., D.G. Golder, J.D. Mahlman and S. Miyahara, 1989: The effect of horizontal resolution on gravity waves simulated by the GFDL SKYHI general circulation model. *Pure Appl. Geophys.*, **130**, 421–443.

Hayashi, Y.-Y. and T. Nakazawa, 1989: Evidence of the existence and eastward motion of superclusters at the equator. *Mon. Wea. Rev.*, **117**, 236–243.

Held, I.M., R.S. Hemler and V. Ramaswamy, 1993: Radiative-convective equilibrium with explicit two-dimensional moist convection. *J. Atmos. Sci.*, **50**, 3909–3927.

Hendon, H.H. and B. Liebmann, 1991: The structure of annual variation of antisymmetric fluctuations of tropical convection and their association with Rossby-gravity waves. *J. Atmos. Sci.*, **48**, 2127–2140.

Hirota, I., 1978: Equatorial waves in the upper stratosphere and mesosphere in relation to the semiannual oscillation of the zonal wind. *J. Atmos. Sci.*, **35**, 714–722.

Hirota, I., 1979: Kelvin waves in the equatorial middle atmosphere observed by the Nimbus 5 SCR. *J. Atmos. Sci.*, **36**, 217–222.

Hitchman, M.H. and C.B. Leovy, 1988: Estimation of the Kelvin wave contribution to the semiannual oscillation. *J. Atmos. Sci.*, **45**, 1462–1475.

Holton, J.R., 1973: On the frequency distribution of atmospheric Kelvin waves *J. Atmos. Sci.*, **30**, 499–501.

Holton, J.R. and R.S. Lindzen, 1972: An updated theory for the quasi-biennial cycle of the tropical stratosphere. *J. Atmos. Sci.*, **29**, 1076–1080.

Itoh, H., 1977: The response of equatorial waves to thermal forcing. *J. Meteor. Soc. Japan*, **55**, 222–239.

Itoh, H. and M. Ghil, 1988: The generation mechanism of mixed Rossby-gravity waves in the equatorial troposphere. *J. Atmos. Sci.*, **45**, 585–604.

Jones, W.L., 1969: Ray tracing for internal gravity waves. *J. Geophys. Res.*, **74**, 2028–2033.

Levy, H.H., J.D. Mahlman and W.J. Moxim, 1982: Tropospheric N_2O variability *J. Geophys. Res.*, **87**, 3061–3080.

Liebmann, B. and H.H. Hendon, 1990: Synopitc-scale disturbances near the equator. *J. Atmos. Sci.*, **47**, 1463–1479.

Lindzen, R.S., 1970: Vertical momentum transport by large-scale disturbances of the equatorial lower stratophere. *J. Meteor. Soc. Japan*, **48**, 81–82.

Lindzen, R.S., 1974: Wave-CISK in the tropics. *J. Atmos. Sci.*, **31**, 156–179.

Lindzen, R.S. and J.R. Holton, 1968: A theory of the quasi-biennial oscillation. *J. Atmos. Sci.*, **25**, 1095–1107.

Lindzen, R.S. and Matsuno, 1968: On the nature of large-scale wave disturbances in the equatorial lower stratosphere. *J. Meteor. Soc. Japan*, **46**, 215–221.

Madden R.A., 1978: Further evidence of traveling planetary waves. *J. Atmos. Sci.*, **35**, 1605–1618.

Madden R.A. and P.R. Julian, 1971: Detection of a 40–50 day oscillation in the zonal wind in the tropical Pacific. *J. Atmos. Sci.*, **28**, 702–708.

Madden R.A. and P.R. Julian, 1972: Description of global-scale circulation cells in the tropics with a 40–50 day period. *J. Atmos. Sci.*, **29**, 1109–1123.

Madden R.A. and P.R. Julian, 1994: Observations of the 40–50-day tropical oscillation — A review. *Mon. Wea. Rev.*, **122**, 814–837.

Mahlman, J.D. and R.W. Sinclair, 1980: Recent results from the GFDL troposphere-stratosphere-mesosphere general circulation model. *Collection of Extended Abstracts Presented at ICMUA Sessions and IUGG Symposium 18*, IAMAP, Boulder, 11–18.

Mahlman, J.D. and L.J. Umscheid, 1984: Dynamics of the middle atmosphere: Success and problems of the GFDL "SKYHI" general circulation model. *Dynamics of the Middle Atmosphere*, J.R. Holton and T. Matsuno, Eds. Terra Scientific, 501–525.

Mahlman, J.D. and L.J. Umscheid, 1987: Comprehensive modeling of the middle atmosphere. The influence of horizontal resolution. *Transport Processes in the Middle Atmosphere*, G. Visconti and R. Garcia, Eds., E. Reidel, 251–266.

Manabe, S., J. Smagorinsky and R.F. Strictler, 1965: Simulated climatology of a general circulation model with a hydrologic cycle. *Mon. Wea. Rev.*, **93**, 769–798.

Manzini, E. and Hamilton, 1993: Middle atmospheric traveling waves forced by latent heat and convective heating. *J. Atmos. Sci.*, **50**, 2180–2200.

Maruyama, T., 1967: Large-scale disturbances in the equatorial lower stratosphere. *J. Meteor. Soc. Japan*, **45**, 391–408.

Maruyama, T., 1968: Upward transport of westerly momentum due to large-scale disturbances in the equatorial lower stratophere. *J. Meteor. Japan*, **46**, 404–417.

Maruyama, T., 1969: Long-term behavior of Kelvin waves and mixed Rossby-gravity waves. *J. Meteor. Soc. Japan*, **47**, 245-254.

Maruyama, T., 1991: Annual and QBO-synchronized variations of lower-stratospheric equatorial wave activity over Singapore during 1961–1989. *J. Meteor. Soc. Japan*, **69**, 219–232.

Maruyama, T., 1994: Upward transport of westerly momentum due to disturbances of the equatorial lower stratosphere in the period range of about 2 days — A Singapore data analysis for 1983–1993. *J. Meteor. Soc. Japan*, **72**, 423–432.

Matsuno, T., 1966: Quasi-geostrophic motions in the equatorial area. *J. Meteor. Soc. Japan*, **44**, 25–43.

Miyahara, S., Y. Hayashi and J.D. Mahlman, 1986: Interaction between gravity waves and planetary-scale flow simulated by the GFDL SKYHI general circulation model. *J. Atmos. Sci.*, **43**, 1844–1861.

Murakami, M., 1979: Large-scale aspects of deep convective activity over the GATE area. *Mon. Wea. Rev.*, **107**, 994–1013.

Nakazawa, T., 1988: Tropical super clusters within intraseasonal variations over the western Pacific. *J. Meteor. Soc. Japan*, **66**, 823–839.

Neelin, J.D., I.M. Held and K.H. Cook, 1987: Evaporation-wind feedback and low-frequency variability in the tropical atmosphere. *J. Atmos. Sci.*, **44**, 2341–2348.

Nitta, T., 1970: A study of generation and conversion of eddy available potential energy in the tropics. *J. Meteor. Soc. Japan*, **48**, 524–528.

Nitta, T., 1972: Energy budget of wave disturbances over the Marshall Islands during the years of 1956 and 1958. *J. Meteor. Soc. Japan*, **50**, 71–84.

Ploshay, J., R. White and K. Miyakoda, 1983: *FGGE III-b daily global analyses. Part I.* NOAA Rep. ERL GFDL 1, U.S. Dept. of Commerce, 278 pp.

Randel, W., 1992: Upper tropospheric equatorial waves in ECMWF analyses. Quart. *J. Roy. Meteor. Soc.*, **118**, 365–394.

Randel, W., B.A. Boville and J.G. Gille, 1990: Observations of planetary mixed Rossby-gravity waves in the upper stratosphere. *J. Atmos. Sci.*, **47**, 3092–3099.

Salby, M.L., and R.R. Garcia, 1987: Transient response to localized episodic heating in the tropics. Part I: Excitation and short-time near field behavior. *J. Atmos. Sci.*, **44**, 458–498.

Salby, M.L., D.L. Hartmann, P.L. Baily and J.C. Gille, 1984: Evidence for equatorial Kelvin modes in Nimbus 7 LIMS. *J. Atmos. Sci.*, **41**, 220–235.

Sassi, F., R.R. Garcia and B.A. Boville, 1993: The stratopause semiannual oscillation in the NCAR community climate model. *J. Atmos. Sci.*, **50**, 3608–3624.

Takahashi, M., 1984: A 2-dimensional numerical model of the semi-annual zonal wind oscillation. *J. Meteor. Soc. Japan*, **62**, 52–67.

Takahashi, M., 1987: A theory of the slow phase speed of the intraseasonal oscillation using the wave-CISK. *J. Meteor. Soc. Japan*, **65**, 43–49.

Takahashi, M., 1993: A QBO-like oscillation in a two-dimensional model derived from a GCM. *J. Meteor. Soc. Japan*, **71**, 641–654.

Takahashi, M. and B.A. Boville, 1992: A three-dimensional simulation of the equatorial quasi-biennial oscillation. *J. Atmos. Sci.*, **49**, 1020–1035.

Takahashi, M. and M. Shiobara, 1994: A note on a QBO-like oscillation in the 1/5 sector CCSR/NIES GCM. *J. Meteor. Soc. Japan*, **72** (in press).

Takayabu, Y.N., 1994a: Large-scale cloud disturbances associated with equatorial waves. Part I: Spectral feature of the cloud disturbances. *J. Meteor. Soc. Japan*, **72**, 433–449.

Takayabu, Y.N., 1994b: Large-scale cloud disturbances associated with equatorial waves. Part II: Westward-propagating inertio-gravitiy waves. *J. Meteor. Soc. Japan*, **72**, 451–465.

Takayabu, Y.M. and T. Nitta, 1993: 3–5 day period disturbances coupled with convection over the tropical Pacific Ocean. *J. Meteor. Soc. Japan*, **71**, 221–246.

Tsay, C.-Y., 1974: Analysis of large-scale wave disturbances in the tropics simulated by an NCAR global circulation model. *J. Atmos. Sci.*, **31**, 330–339.

Wallace, J.M., 1971: Spectral studies of tropospheric wave disturbances in the tropical western Pacific. *Rev. Geophys. Space Phys.*, **9**, 557–612.

Wallace, J.M., 1973: General circulation of the tropical lower stratosphere. *Rev. Geophys. Space Phys.*, **11**, 191–222.

Wallace, J.M. and V.E. Kousky, 1968: Observational evidence of Kelvin waves in the tropical stratosphere. *J. Atmos. Sci.*, **25**, 280–292.

Yanai, M., 1975: Tropical meteorology. *Rev. Geophys. Space Phys.*, **13**, 685–710 and 800–808.

Yanai, M. and Y. Hayashi, 1969: Large-scale equatorial waves penetrating from the upper troposphere into the lower stratosphere. *J. Meteor. Soc. Japan*, **47**, 167–182.

Yanai, M. and M.-M. Lu, 1983: Equatorially trapped waves at the 200 mb level and their association with meridional convergence of wave energy flux. *J. Atmos. Sci.*, **40**, 2785–2803.

Yanai, M. and T. Maruyama, 1966: Stratospheric wave disturbances propagating over the equatorial Pacific. *J. Meteor. Soc. Japan*, **44**, 291–294.

Yanai, M. and M. Murakami, 1970a: A further study of tropical wave disturbances by the use of spectrum analysis. *J. Meteor. Soc. Japan*, **48**, 186–197.

Yanai, M. and M. Murakami, 1970b: Spectrum analysis of symmetric and antisymmetric equatorial waves. *J. Meteor. Soc. Japan*, **48**, 186–197.

Yanai, M., T. Nitta and Y. Hayashi, 1968: Power spectra of large-scale disturbances over the tropical Pacific. *J. Meteor. Soc. Japan*, **46**, 308–323.

Zangvil, A. and M. Yanai, 1980: Upper tropospheric waves in the tropics. Part I: Dynamical analysis in the wavenumber-frequency domain. *J. Atmos. Sci.*, **37**, 283–298.

Zangvil, A. and M. Yanai, 1981: Upper tropospheric waves in the tropics. Part II: Association with clouds in the wavenumber-frequency domain. *J. Atmos. Sci.*, **38**, 939–953.

GFDL "SKYHI"大気大循環モデルと FGGE データセットに現われるケルビン波と混合ロスビー重力波: それらの生成メカニズムと QBO における役割

林　良一・D.G. Golder
(プリンストン大学地球流体力学研究所)

赤道ケルビン波と混合ロスビー重力 (MRG) 波のシミュレーションと理論を評価するため、またそれらの生成メカニズムと準二年周期振動における役割への洞察を得るため、時空間スペクトル解析を 40 層、緯度 3 度、経度 3.6 度の GFDL"SKYHI"大気大循環モデルからの output データと GFDL FGGE データセットに行った。

SKYHI と FGGE の成層圏ケルビン波はともに、下部成層圏において東進、波数 1 、10–20 日周期成分が卓越する。これらの波は高い波数—振動数成分を伴っており、これらは下部成層圏よりも上部成層圏において明瞭に検出される。一方、SKYHI と FGGE の MRG 波は、西進、波数 3–5 、4–6 日成分が下部成層圏で卓越する。上部成層圏においてこれらの波は、さらに低い波数 (1–2) 、短い周期 (2–4 日) 成分が卓越する。SKYHI/FGGE ケルビン波と MRG 波の振幅は、観測された (非 FGGE) 地点データから見積られるものに匹敵するが、SKYHI モデルは弱い準二年周期成分しか生成しない。SKYHI 降水データは降水のグリッドサイズのパルスを断続的に示すが、ケルビン波と MRG 波に対応する明瞭なスペクトルピークを示さない。

本解析に基づき、ケルビン、MRG および重力波は、波—対流相互作用の結果生じ、対流加熱のランダムパルスにより断続的に引き起こされるという生成機構を提案する。準二年周期振動は重力波によって第一に生成され、モデルにおける水平分解度が増すと対流加熱のグリッドサイズパルスと小規模重力波が適宜生成されるので、振幅が増大すると考えられる。